UC Davis
UC Davis Previously Published Works

Title

Ca2+ signaling in T lymphocytes: the interplay of the endoplasmic reticulum, mitochondria, membrane potential, and CRAC channels on transcription factor activation

Permalink

Journal

ISSN

Authors

Yang, Pei-Chi
Jafri, M Saleet

Publication Date

DOI

Peer reviewed

Contents lists available at ScienceDirect

Heliyon

Research article

Ca^{2+} signaling in T lymphocytes: the interplay of the endoplasmic reticulum, mitochondria, membrane potential, and CRAC channels on transcription factor activation

Pei-Chi Yang [a,b], M. Saleet Jafri [b,c,*]

[a] Department of Physiology and Membrane Biology, University of California Davis, Davis, CA, 95616, USA
[b] Krasnow Institute for Advanced Study and School of Systems Biology, George Mason University, Fairfax, VA, 22030, USA
[c] Center for Biomedical Engineering and Technology, University of Maryland School of Medicine, Baltimore, MD, 20201, USA

ARTICLE INFO

ABSTRACT

T cell receptor stimulation initiates a cascade of reactions that cause an increase in intracellular calcium (Ca^{2+}) concentration mediated through inositol 1,4,5-trisphosphate (IP$_3$). To understand the basic mechanisms by which the immune response in T cells is activated, it is useful to understand the signaling pathways that contain important targets for drugs in a quantitative fashion. A computational model helps us to understand how the selected elements in the pathways interact with each other, and which component plays the crucial role in systems. We have developed a mathematical model to explore the mechanism for controlling transcription factor activity, which regulates gene expression, by the modulation of calcium signaling triggered during T cell activation. The model simulates the activation and modulation of Ca^{2+} release-activated Ca^{2+} (CRAC) channels by mitochondrial dynamics and depletion of endoplasmic reticulum (ER) store, and also includes membrane potential in T-cells. The model simulates the experimental finding that increases in Ca^{2+} current enhances the activation of transcription factors and the Ca^{2+} influx through CRAC is also essential for the NFAT and NFκB activation. The model also suggests that plasma membrane Ca^{2+}-ATPase (PMCA) controls a majority of the extrusion of Ca^{2+} and modulates the activation of CRAC channels. Furthermore, the model simulations explain how the complex interaction of the endoplasmic reticulum, membrane potential, mitochondria, and ion channels such as CRAC channels control T cell activation.

1. Introduction

In many cells, the interplay of calcium (Ca^{2+}) uptake and release processes results in oscillations in the intracellular Ca^{2+} concentration when surface receptors are stimulated by agonist [1]. As diagrammed in Figure 1A, the binding of antigen-MHC (major histocompatibility complex) complexes to the T cell receptor (TCR) results in the activation of a tyrosine kinase that phosphorylates phospholipase C-gamma (PLC-γ) causing its activation. Activated PLC-γ cleaves phosphatidyl inositol (PIP$_2$) in the plasma membrane into two parts, diacylglycerol (DAG) and inositol 1,4,5-triphosphate (IP$_3$). The molecule DAG remains in the plasma membrane and activates protein kinase C (PKC). IP$_3$, in contrast, is a diffusible cytosolic messenger, which binds to the IP$_3$ receptor on the endoplasmic reticulum (ER) and synergistically with Ca^{2+} causes Ca^{2+} release from the ER. The ER is refilled by the sarcoplasmic and
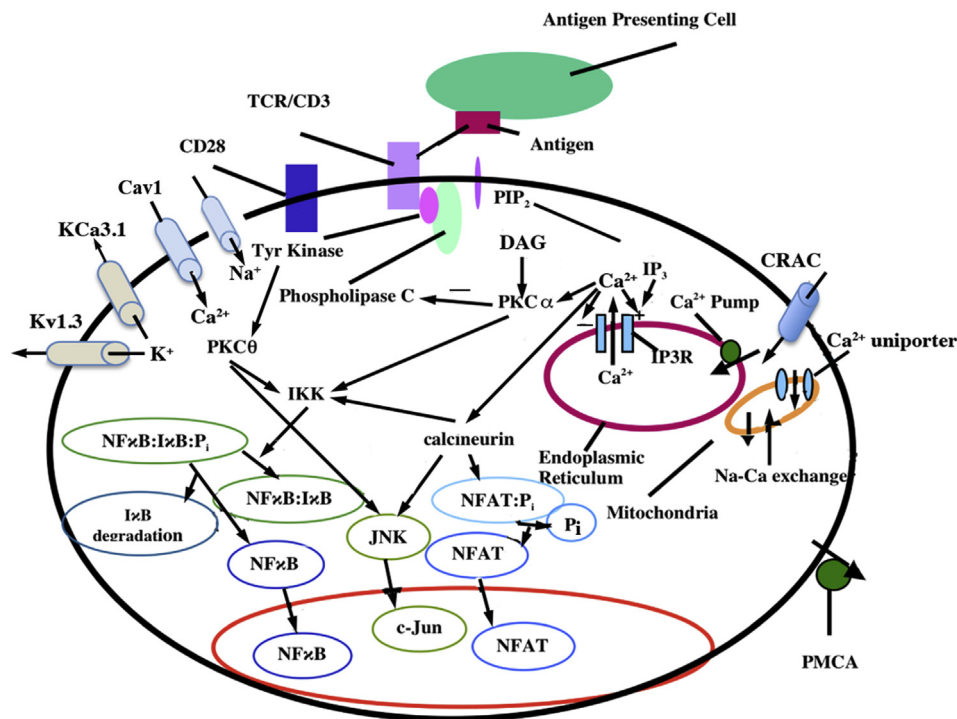
endoplasmic reticulum Ca^{2+}-ATPases (SERCA) pump [2]. In addition, there are also other membrane ion channels, voltage-dependent calcium (Cav1) and voltage- (Kv1.3) [3,4] and calcium-dependent potassium channels (I$_{K(Ca)}$, KCa3.1) [4, 5, 6], that maintain the membrane potential [7, 8].

Many studies have indicated that Ca^{2+} release-activated Ca^{2+} (CRAC) channels are responsible for Ca^{2+} influx, and that plasma membrane Ca^{2+}-ATPases (PMCA) play a major role in removal of Ca^{2+} in T cells [9]. In addition, mitochondria can modulate the Ca^{2+} influx by reducing the Ca^{2+}-dependent inactivation of CRAC channels [10]. The Ca^{2+} ion is a signaling molecule that binds to and activates the phosphatase calcineurin, which in turn binds to and dephosphorylates NFAT (nuclear factor – activated T cells) [11, 12, 13, 14]. Dephosphorylation exposes nuclear localization signals on NFAT [15], resulting in rapid translocation of the NFAT-calcineurin complex to the nucleus where it can
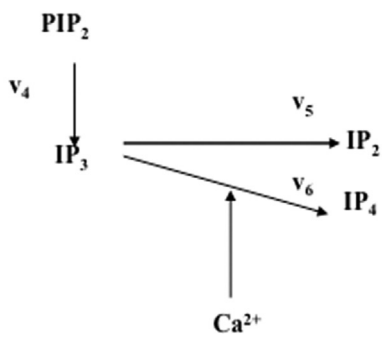
A

B

C

Figure 1. Schematic diagram for T cell activation and mechanism of IP$_3$ activation. (A) Schematic diagram of the mechanism of Ca^{2+} dynamics in T-cells. (B) IP$_3$ activation pathway. (C) The model of IP$_3$R/channel subunit [78]. Each subunit represents an IP$_3$ binding site, activating and inactivating Ca^{2+} binding site. Each state is labeled X$_{ikj}$, where i (IP$_3$ binding site), j (activating Ca^{2+} binding site) and k (inactivating Ca^{2+} binding site) are equal to 0 (unoccupied binding site) or 1 (occupied binding site) [78].
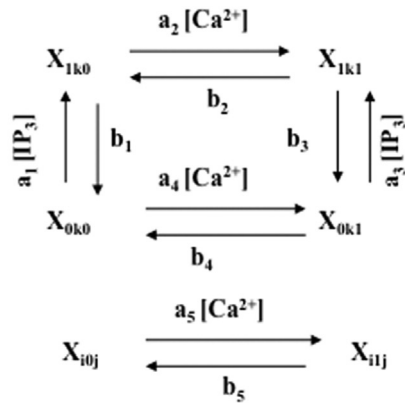
participate in promoting gene transcription [16]. In contrast to NFAT, NFκB is retained in the cytoplasm not by phosphorylation but by association with the inhibitory IκB protein [17]. Increasing Ca^{2+} and activated PKCθ co-activate Iκ kinase (IKK) and phosphorylates IκB associated with NFκB allowing the IκB to dissociate from NFκB and marking the IκB for subsequent polyubiquitination and degradation by the proteasome [18, 19]. The free NFκB is translocated to the nucleus where it can bind to DNA and promote gene transcription. Moreover, in the related c-Jun NH$_2$-terminal kinase (JNK) pathway, PKCθ mediates the activation of c-Jun (Figure 1A). PKC-θ is induced by co-stimulation of TCR/CD3 and CD28. Several studies show that PKCθ regulates the mitogen-activated protein kinase (MAP kinase) cascade, SEK1/MKK4 that directly phosphorylate JNK [20, 21]. Ca^{2+} activated calcineurin also activates on SEK1. Integration of these two activities reaches the full activation of JNK [22]. As in result, activated JNK phosphorylates two positive regulatory

serine residues in the activation domain of c-Jun. Finally, c-Jun and c-Fos protein together forms the activator-protein 1 (AP-1) transcription factors complex that participate in cell growth [23].

Our previous model simulated the calcium clamp protocol used in the *in vitro* experiments used by Dolmetsch and co-workers; *in vivo*, however, the T cell has more complex calcium dynamics [24, 25]. The calcium dynamics model presented here explores how the interplay between Ca^{2+} influx through CRAC channels, the mitochondria, the plasmalemmal Ca^{2+}-ATPase (PMCA) pump, and ER stores work together to control cytosolic calcium concentration ([Ca^{2+}]$_{cyt}$) dynamics and how membrane currents affect the calcium dynamics. This novel model includes the following features: 1) a mechanistic description of the cytosolic Ca^{2+} dynamics that relies on local Ca^{2+} signaling based on the experimental data of Bautista and co-workers [26]; 2) IP$_3$ production and degradation based on the work of Swillens and Mercan [27]; 3) A novel description of

the CRAC channel; 4) a description of the PMCA pump based on the experimental kinetics observed by Bautista and co-workers [26]; 5) a description of the membrane potentials and the ion channels that regulate it 6) a voltage-dependent potassium channel (Kv1.3) based on the experimental data of Dupuis et al. [28]; 7) a calcium-dependent potassium channel based upon the data of Verheugen et al. [29]; 8) a description of the TRPM4 channel by Gaur et al. [30]; 9) a new formulation of the TRPC3 channel based on the experimental data of Rose et al. [31].; 10) the Cl^- channel based on data by Feske [8] 11) the L-type Ca^{2+} channel description by Luo and Rudy [32]; and a Na^+ channel description by Luo and Rudy [32].

Defects in the activation of NFAT and expression of IL-2 have been implicated in a number of human diseases and conditions. In several patients, failure to activate NFAT was shown to cause severe combined immunodeficiency disease, SCID [8]. In contrast, a number of studies have suggested that active NFAT from patients infected by human immunodeficiency virus 1 (HIV-1) or human T-cell lymphotropic virus type-1 (HTLV-1) boost the viral infectivity [33]. The NFAT pathway is also an important target for drugs such as FK506 and cyclosporine A, both powerful immunosuppressants that block the activation of calcineurin's phosphatase activity [34, 35, 36]. While these drugs are useful for preventing the rejection of transplanted tissues, immune system suppression can lead to severe side effects, such as secondary tumors and opportunistic infections [37], and progressive loss of renal function and neurotoxicity [38]. In addition, inhibition of transcription factor activation in other types of cells can have unintended and undesirable consequences [39].

A quantitative understanding of the mechanisms of T cell activation would help to predict the underlying mechanisms and suggest possible targets for drug intervention. Therefore, computational models are useful to understand the complex Ca^{2+} dynamics in transcription factors activation pathways both to find better ways to control the immune system in transplant patients and to find therapies for immunodeficiency viral infections.

2. Results

Using the parameter values in Tables 1, 2, 3, 4, 5, 6, and 7, the model under resting conditions reached steady state variable values shown in Table 8. After 1000 s at rest, the variable stay near the initial values with the membrane potential within the experimental range of 50–60 mV assuming the value of 59.0 mV at rest [7, 8]. Calcium concentrations for cytoplasmic (0.089 μM), endoplasmic (335.8 μM), and mitochondrial (0.00054 μM) calcium also fall within experimental ranges [7, 8, 40].

Figure 2 presents simulations of cytosolic and endoplasmic reticulum calcium concentrations and fluxes. In these simulations, the extracellular calcium concentration ($[Ca^{2+}]_o$) was set to 2.0 mM from 420 s to 800 s and 0.0 mM otherwise. Increasing levels of agonist stimulation are assumed to result in increasing PLC activity in accordance with experimental studies on T cell receptor activation and PLC activity [41]. The application of agonist (indicated by the gray bar in Figure 2A) is simulated by increasing the rate of IP_3 production (and DAG) from PIP_2 by

phospholipase C (v_4) from 0.05 μM s^{-1} to 5.0 μM s^{-1} after 64 s. The simulated traces for cytosolic $[IP_3]$ and [DAG] are shown in Figure 3. Simulated cytosolic calcium concentration is shown in Figure 2A. After the simulated application of agonist, there is a transient increase in $[Ca^{2+}]_{cyt}$. After the addition of 2.0 mM $[Ca^{2+}]_o$, a larger increase from baseline to a ~1.5 μM, followed by a slow decrease to a plateau of approximately 1.0 μM is observed. These results agree with the results observed by Bautista and co-workers [26]. The time course of $[Ca^{2+}]_{SS}$ is similar to that of $[Ca^{2+}]_{cyt}$ except that the plateau of the second transient is larger in amplitude (Figure 2B). The cytosolic Ca^{2+} transients are accompanied by mitochondrial Ca^{2+} transients that are significantly larger in amplitude shown in Figure 2C. Figure 2D shows an initial depletion of $[Ca^{2+}]_{ER}$ as Ca^{2+} is released from the ER store in response to agonist. During the Ca^{2+} transients, the model predicts that PMCA switches from the unmodulated (Figure 2E; red line) to the modulated state (Figure 2E; black line) whenever $[Ca^{2+}]_{cyt}$ is elevated above the resting level.

Figure 4 shows plasma membrane current responses in the simulations from Figure 2. As suggested by the Bautista, the model also predicts that the transient rise in cytosolic Ca^{2+} after the reintroduction of extracellular calcium is due to Ca^{2+} entry through the CRAC channel (Figure 4A). Ca^{2+} entry is accompanied by membrane hyperpolarization (Figure 4B), as observed by Tsien and co-workers [42]. The depolarizing influence of the CRAC current is opposed by Ca^{2+} triggered opening K^+ channels (Figure 4C) which contributes to hyperpolarization in Figure 4B, as well as by the opening of voltage-dependent K^+ channels (Figure 4D). The TRPC3 channel opens in response to an increase in DAG to allow Ca^{2+} entry (Figure 4E). The TRPM4 channel conducts Na^+ and K^+ and is activated by Ca^{2+} (Figure 4F).

Bautista and colleagues [26] suggested that mechanisms of Ca^{2+} clearance from the cytosol include the PMCA, mitochondria, and SERCA. To investigate this proposal, four different simulations were performed with the model (Figures 5, 6, and 7). The following protocol used by Bautista and colleagues was used for each of these simulations: $[Ca^{2+}]_o$ was set to 2.0 mM for 15 s and 40 s as indicated by the black bars above the graphs and held at 0.0 mM otherwise. Agonist was simulated by increasing the IP_3 production rate from 0.01 μM s^{-1} to 5 μM s^{-1} after 64 s indicated by the gray bar. In their experiments, oligomycin/antimycin was added to block mitochondrial Ca^{2+} uptake to test the role of the mitochondria. To test the role of the ER, Ca^{2+} uptake was blocked by incubation with thapsigargin. Finally, both oligomycin/antimycin and thapsigargin were added to the incubation medium to simulate blocking of both mitochondrial and ER uptake of Ca^{2+}.

The control (Figure 5A) shows that after the addition of agonist there is an initial elevation of $[Ca^{2+}]_{cyt}$, followed by a second and a third cytosolic Ca^{2+} transient during the 15 s and 40 s intervals of raised $[Ca^{2+}]_o$. The next set of simulations tests the role of mitochondria by blocking mitochondrial Ca^{2+} uptake (Figure 5B). To simulate this hypothesis, the fluxes through the Ca^{2+} uniporter and mitochondrial membrane potential (Ψ_m) were set to 0. As in the control, Figure 5A, 2.0 mM $[Ca^{2+}]_o$ was applied for 15 s and 40 s. In this case (Figure 5B), the first transient elevations of $[Ca^{2+}]_{cyt}$ are slightly higher than control

Table 1. IP_3 and DAG production and degradation parameters.

Parameters	Definition	Values	Reference
v_4	Maximal rate of IP_3 and DAG formation by PLC	5.0 μM s^{-1}	Scaled from [27]
v_5	Maximal rate of IP_3 dephosphorylation	12.5 μM s^{-1}	Scaled from [27]
v_6	Maximal rate of IP_3 phosphorylation	0.9 μM s^{-1}	Scaled from [27]
K_5	IP_3 dissociation constant	6.0 μM	Scaled from [27]
K_6	IP_3 dissociation constant	0.1 μM	Scaled from [27]
K_7	Ca^{2+} dissociation constant	1.0 μM	Scaled from [27]
H	Hill coefficient	1	[27]
v_8	DAG degradation rate	1.0 s^{-1}	Estimated

Table 2. Ca^{2+} Regulatory Mechanism Parameters and Binding Constants of IP_3 receptor.

Parameters	Definition	Values	Reference
v_1	Maximum IP_3 receptor flux	90 s^{-1}	Rescaled from [78]
a_1	IP_3 binding constant	$400 \text{ μM}^{-1} \text{ s}^{-1}$	[78]
a_2	Ca^{2+} inhibitory receptor binding constant	$0.2 \text{ μM}^{-1} \text{ s}^{-1}$	[78]
a_3	IP_3 binding constant	$400 \text{ μM}^{-1} \text{ s}^{-1}$	[78]
a_4	Ca^{2+} Inhibitory receptor binding constant	$0.2 \text{ μM}^{-1} \text{ s}^{-1}$	[78]
a_5	Ca^{2+} activation receptor binding constant	$20.0 \text{ μM}^{-1} \text{ s}^{-1}$	[78]
d_1	IP_3 dissociation constant	0.13 μM	[78]
d_2	Ca^{2+} Inhibitory receptor dissociation constant	1.049 μM	[78]
d_3	IP_3 dissociation constant	0.9434 μM	[78]
d_4	Ca^{2+} Inhibitory receptor dissociation constant	0.1445 μM	[78]
d_5	Ca^{2+} activation receptor dissociation constant	82.34 nM	[78]
v_{SERCA}	Maximal velocity for SR Ca^{2+} ATPase	1.0 μM s^{-1}	[2, 78]
K_{serca}	Ca^{2+} dissociation constant for SR Ca^{2+} ATPase	0.1 μM	[2, 78]
τ_{sscyt}	Transfer time constant between subspace and cytosol	0.5 s	Estimated

Table 3. Ca^{2+} buffering parameters.

Parameters	Definition	Values	Reference
$[B_s]_{cyt}$	Total cytosolic stationary buffer concentration	225.0 μM	[2]
$[B_s]_{ss}$	Total subspace stationary buffer concentration	5.0 mM	
$[B_s]_{ER}$	Total stationary buffer concentration in the ER	2.0 mM	[2]
$[B_e]_{cyt}$	Total cytoplasmic buffer concentration in the cytosol	111.0 μM	[2]
$[B_e]_{SS}$	Total buffer concentration in the subspace	111.0 μM	Same as $[B_e]_{cyt}$
$[B_e]_{ER}$	Total buffer concentration in the ER	111.0 μM	Same as $[B_e]_{cyt}$
K_s^{ER}	Stationary buffer dissociation constant in ER	1.0 μM	[2]
K_s^{cyt}	Cytosolic stationary buffer dissociation constant for Ca^{2+}	0.1 μM	[2]
K_s^{ss}	Subspace stationary buffer dissociation constant for Ca^{2+}	0.1 μM	Same as K_s^{cyt}
K_e^{cyt}	Mobile cytoplasmic buffer dissociation constant for Ca^{2+} in the cytosol	0.123 μM	[26]
K_e^{ss}	Mobile buffer dissociation constant for Ca^{2+} in the subspace	0.123 μM	Same as K_e^{cyt}
K_e^{ER}	Mobile buffer dissociation constant for Ca^{2+} in the ER	0.123 μM	Same as K_e^{cyt}

Table 4. Parameters of mitochondrial dynamics.

Parameters	Definition	Values	Reference
P_{UNI}	Uniporter Ca^{2+} permeability	$2.776 \times 10^{-14} \text{ s}^{-1}$	Estimated
α_m	Mitochondrial Ca^{2+} activity coefficient	0.2	[89]
α_{ss}	Subspace Ca^{2+} activity coefficient	1.0	Fit to [26]
V_{nc}	Na^+-Ca^{2+} exchanger maximal velocity	1.836 μM s^{-1}	Estimated
K_{Na}	Na^+-Ca^{2+} exchanger Na + affinity	8.0 mM	[90]
K_{Ca}	Na^+-Ca^{2+} exchanger Ca^{2+} affinity	8 μM	[90]
Ψ_m	Mitochondrial membrane potential	160 mV	[91]
$[Na^+]_{SS}$	Extramitochondrial Na^+ concentration	5.0 mM	[32]
$[Na^+]_m$	Mitochondrial Na^+ concentration	5.0 mM	Estimated
β_{Ca}	Ca^{2+} buffers in the mitochondria.	0.01	[92]

(Figure 5A) and the third transient elevations of $[Ca^{2+}]_{cyt}$ are noticeably higher than control (Figure 5A). To determine the effects of the ER on Ca^{2+} clearance dynamics, simulations with a disabled SERCA pump ($J_{SERCA} = 0$) were performed (Figure 5C). In these simulations the initial $[Ca^{2+}]_{cyt}$ transient is mostly abolished and the third transient is slightly larger. Finally, when both mitochondrial and ER uptake of Ca^{2+} are blocked (Figure 5D) by combining the protocols used in Figures 5B and 5C, the first transient is abolished, and the third transients are higher than the control. These results agree with the experimental observations [26]. In all cases the second transients are slightly bigger than the control, also similar to experiments.

Studies have been shown that the main sources of Ca^{2+} that produce $[Ca^{2+}]_{cyt}$ transients in T lymphocytes are released from the ER through the IP_3 receptor, and Ca^{2+} influx into the cell through the CRAC channel from the extracellular space [9, 43]. Figure 6A, B shows these Ca^{2+} currents for the four cases shown in Figure 5: control (black line), disabled mitochondrial Ca^{2+} uptake (red line), blocked SERCA pump (green line), and disabled both mitochondria and SERCA (blue line). The first transient after application of agonist is due entirely to release from the ER through the IP_3 receptor (Figure 6A) for the control case (black solid line) and the case with blocked mitochondria (red). There is attenuated release from the ER in the cases with the SERCA blocked

Table 5. Parameters of I_{CRAC} channel and PMCA pump.

Parameters	Definition	Values	Reference
V_u	Unmodulated PMCA velocity	$1.54 \times 10^6\ s^{-1}$	[26]
K_u	Dissociation constant for Ca^{2+} stimulation of unmodulated PMCA	303.0 nM	[26]
V_m	Modulated PMCA velocity	$2.20 \times 10^6\ s^{-1}$	[26]
K_m	Dissociation constant for Ca^{2+} stimulation of modulated PMCA	140.0 nM	[26]
K_{inact}	Dissociation constant for ORAI1 Ca^{2+} inhibition by CRACR2A	0.8 μM	Estimated
K_{cc}	Dissociation constant for time constant for ORAI1 inhibition by calmodulin	2.0 μM	Estimated
K_{act}	Dissociation constant for ER Ca^{2+} inhibition	200.0 μM	Estimated
τ_{inact}	J_{CRAC} inactivation time constant	40 s	[10]
τ_{act}	J_{CRAC} activation time constant	3 s	[93]
α_{SS}	Subspace Ca^{2+} activity coefficient	1.0	Fit to [26]
α_o	Extracellular Ca^{2+} activity coefficient	0.341	Fit to [26]
P_{CRAC}	CRAC permeability to Ca^{2+}	$2.8 \times 10^{-10}\ cm^3/s$	Estimated

Table 6. General parameters.

Parameters	Definition	Values	Reference
z	Valence of Ca^{2+}	2	Physical constant
F	Faraday's constant	96484.6 coul (mol e$^-$)$^{-1}$	Physical constant
R	Ideal gas constant	8314 mJ mol^{-1} K^{-1}	Physical constant
T	Absolute temperature	310 K	Body temp
V_T	T cell volume	2 pl	[26]
V_{cyt}	Cytosol volume	1.1 pl	[94]
V_{SS}	Subspace volume	0.11 pl	[94]
V_{ER}	ER volume	0.011 pl	[94]
V_{mito}	Mitochondrial matrix volume	0.088 pl	[94]

Table 7. –Membrane currents parameters.

Parameters	Definition	Values	Reference
E_{max}	Maximum conductance for Ca^{2+}-dependent K^+ channel	0.8 nS	[6, 29]
K_d	Ca^{2+} dissociation constant for Ca^{2+}-dependent K^+ channel	0.45 μM	[29]
g_t	Maximum conductance of the K^+ channels	3.0 nS	[6]
E_K	Reversal potential of K^+	-84 mV	[6, 95]
g_{Cl}	Maximum conductance of the background current	0.07 nS	Estimated
E_{Cl}	Reversal potential for Cl$^-$	-33.0 mV	[95]
g_{Na}	Maximum conductance of the Na + channels	3.0 nS	Estimated
E_{Na}	Reversal potential of K+	-70 mV	[6, 95]
C_m	Membrane capacitance	2.5e-3 nF	[94]
E_{Ca}	Reversal potential of Ca^{2+}	60 mV	[6, 95]
PcaL	L-type Ca^{2+} channel permeability	$0.3 \times 10^{-7}\ cm^2 s^{-1}$	[32]
g_{TRPC3}	Maximum conductance of TRPC3 channels	0.00195 nS	Estimated
K_{DAG}	DAG binding constant for TRPC3 activation	2.0 μM	Estimated
E_{TRPM4}	TRPM4 reversal potential	0.2 mV	[30]
g_{TRPM4}	Maximum conductance of TRPM4 channels	1.2 nS	Estimated
τ_{xCa}	Hodgkin-Huxley time constant TRPM4 channel	30 s	[30]

(green and blue lines overlapping). Release through the IP$_3$ receptor contributes significantly to the second and third transient in all cases as the opening of CRAC channels provides Ca^{2+} to trigger Ca^{2+} release from the IP$_3$ receptor, which is possible in the presence of IP$_3$. There is a large CRAC current during both the second and third Ca^{2+} transients (Figure 6B). The behavior of the activation and inactivation "gates" for the CRAC channel which shown in Figure 6C, D. The activation of the CRAC channel is controlled by ER concentrations (Figure 6C). In the control case and case with the mitochondria blocked, the ER is full until application of agonist at which point the $[Ca^{2+}]_{ER}$ declines. When the ER is full the activation gate of the CRAC channel is near 0. When the ER

depletes it rises to above 0.5. In the cases with the ER is blocked (green and blue lines), the activation gate of the CRAC channel starts the simulation partially activated and quickly rises for the duration of the simulation (Figure 6C). Note that in all cases for the second and third transients the CRAC activation gates are open, suggesting that activation of the CRAC channel is not responsible for the changes of I$_{CRAC}$ seen in Figure 6B. Figure 6D shows the behavior of the CRAC inactivation by $[Ca^{2+}]_{SS}$. In all cases and with all transients, the CRAC activation gates are off at the beginning of the simulation (i.e. equal to 1). For the second transients, all cases are similar. However, for the third transients, CRAC currents are prolonged and slowly decrease. The downward deflections

Table 8. Steady-state values.

Variables	Initial values
$[Ca^{2+}]_{cyt}$	0.089 µM
$[Ca^{2+}]_{ER}$	335.5 µM
$[Ca^{2+}]_m$	0.00054 µM
$[Ca^{2+}]_{ss}$	0.33 µM
V	-58.1 mV
$[IP_3]_{cyt}$	0.018 µM
[DAG]	0.050 µM
X_{100}	0.039
X_{110}	0.042
X_{000}	0.27
X_{010}	0.29
X_{001}	0.17
X_{101}	0.0033
X_{011}	0.18
X_{111}	0.0035
u	0.53
m	0.0898
h	0.0796
n	0.04
j	.08
d	0.00038
f	0.94
x_{Ca}	0.0497
JNK:PKC:Cn	0.00398
$[NFAT:P_i]_c$	0.00957 µM
$[NFAT:C^*]_n$	0.000723 µM
$[NF\kappa B]_n$	49.13 nM
$[NF\kappa B:I\kappa B]_c$	31.69 nM
inact	0.90
proact	0.081

are inversely proportional to the transients in $[Ca^{2+}]_{SS}$. The inactivation gate of CRAC decreased in the four cases (arrow) with the probability described from largest decrease to the smallest decrease block of both SERCA and mitochondria (blue) > being blocked mitochondria (red) > blocked SERCA (green) > control (black). This suggests that the differences in CRAC seen during this protocol are due to differences in CRAC inactivation governed by $[Ca^{2+}]_{SS}$.

To further understand the mechanisms at play, the model was used to predict the Ca^{2+} concentrations in the ER, mitochondria, and subspace. Figure 6 shows all four cases with the same labeling scheme as Figure 6. After the application of agonist, the $[Ca^{2+}]_{ER}$ falls from its resting value of 335.5 µM (Figure 7A) for the control (black line) and the case with blocked mitochondria (red line) due to opening of the IP_3 receptors (shown previously in Figure 6A). In the cases where the SERCA pump is blocked (Figure 7A – green and blue lines overlapping) there is reduced $[Ca^{2+}]$ in the ER, at the start of the simulation. In these cases, the $[Ca^{2+}]_{ER}$ reaches is nadir of approximately 1 µM. During each of the $[Ca^{2+}]_{cyt}$ transients in the cases with functioning mitochondria (Figure 7B – black solid and green lines) there is a transient rise in $[Ca^{2+}]_m$. When SERCA is blocked (Figure 7B – green line), the $[Ca^{2+}]_m$ is smaller in amplitude transient and slightly lower during the first transient but otherwise similar to the control. This can be attributed to the decreased release from the ER seen in Figure 6A. In the cases with the mitochondria Ca^{2+} uptake blocked there is little notable change in $[Ca^{2+}]_m$. From highest to lowest increases in the third transient, are the cases with both SERCA blocked (green) > control (black) > mitochondria and SERCA blocked (blue) > blocked mitochondrial Ca^{2+} uptake (red). The changes in $[Ca^{2+}]_{SS}$ are shown in Figure 7C. When the SERCA is unblocked (black and red lines), the first transient is similar to the

transients in $[Ca^{2+}]_{cyt}$. In the second and third transients, in all cases, there are transients in $[Ca^{2+}]_{SS}$. The difference in the cases is most clear in the third transient where there is prolonged Ca^{2+} entry through CRAC channels. Here the current, in order from highest to lowest (arrow), are the cases with both mitochondria and SERCA blocked (blue) > blocked mitochondrial Ca^{2+} uptake (red) > SERCA blocked (green) > control (black) Note that these are opposite the contributions from CRAC inactivation by $[Ca^{2+}]_{SS}$ shown in the third transient in Figure 6D, indicating a possible role of CRAC channels in this observation.

The model was used to study the importance of I_{CRAC} for activation of NFAT, Ca^{2+} was triggered by the simulated application of agonist in the presence of 0.0 mM $[Ca^{2+}]_o$ to eliminate I_{CRAC} (Figure 8A). The result is an initial transient due to Ca^{2+} release from the ER followed by a return to baseline, and consequently little translocation of NFAT and NFκB (Figures 8C and 8E, respectively) to the nucleus and little JNK activation (Figure 8G). In Figure 8B, $[Ca^{2+}]_o$ was set to 2.0 mM for 1000 s, and 0.0 mM after that. Agonist was added after 200 s. The $[Ca^{2+}]_{cyt}$ increases to peak of approximately 5 µM, then slowly decreases to a plateau of 1.0 µM. When $[Ca^{2+}]_o$ is reduced to 0.0 mM at 1200 s, the $[Ca^{2+}]_{cyt}$ decline back toward baseline. During the simulation protocol NFAT and NFκB (Figures 8D and 8F, respectively) translocate to the nucleus during calcium transient and decline after the $[Ca^{2+}]_{cyt}$ decreases back to baseline Figure 8H shows the percent active JNK in the cytoplasm raises rapidly when PKCθ is activated and Ca^{2+} concentration increase. When Ca^{2+} are fall after 1200 s when agonist stimulation of PLC activation is ended i.e. production of IP_3 returns to baseline), the JNK and NFAT levels fall rapidly and the NFκB declines more slowly. The simulated JNK and the experimental results from Leung and co-workers [44] showing the co-activation by PKCθ and Ca^{2+} is greater than activation by either alone (Figure 9).

The model was used to explore the role of the membrane currents in T lymphocyte activation. Experiments have shown that block of I_K (green) and $I_{K(Ca)}$ (blue) can inhibit T lymphocyte activation [45, 46]. Their expression level differs across different types of T lymphocytes and knockdown experiments have shown that deficiency of I_K can be compensated for by $I_{K(Ca)}$ [47, 48]. Figure 8AC shows that block of $I_{K(Ca)}$ attenuates the Ca^{2+} transient and NFAT translocation to the nucleus. This is due to activation of $I_{K(Ca)}$ during Ca^{2+} entry through the CRAC channel preventing membrane depolarization thereby maintaining the driving force for Ca^{2+} entry. Under the current parameter block of I_K has little effect on T lymphocyte activation. However, if I_K expression was increased so that it played a more significant role in preventing depolarization during Ca^{2+} entry, it would affect T lymphocyte activation.

In the current parameter set, L-type Ca^{2+} expression is low resulting in a small current (Figure 10A). As such it plays a small role in T lymphocyte activation as its block does little to alter the Ca^{2+} transient and NFAT translocation to the nucleus (Figure 11AC - tan). If the L-type current is increased and other currents rebalanced, its block can attenuate T lymphocyte activation. Block of I_{Na} shows little effect on T lymphocyte activation (Figure 11BD - pink). This is because I_{Na} activated during depolarization and not during the peak period of Ca^{2+} entry (Figure 10B).

In model simulation, block of TRPM4 channels results in a slightly increased Ca^{2+} transient and increase in NFAT activation while increase expression of the channel results in a decreased Ca^{2+} transient and decrease in NFAT activation (Figure 11BD – light blue). Increase in TRPM4 results in a decreased Ca^{2+} transient and NFAT (not shown). Experiments have shown that RNAi inhibition of TRPM4 in T cells results in an increase in the magnitude of the Ca^{2+} during activation [49]. TRPM4 channels are activated by Ca^{2+} and the ensuing Na^+ entry through open channels depolarizes the membrane reducing the driving force for Ca^{2+} through other channels such as CRAC [50, 51]. The model confirms this mechanism.

The model was used to explore the role of TRP channels in T lymphocyte activation. Block of TRPC3 attenuates Ca^{2+} entry, which limits NFAT translocation to the nucleus (Figure 11BD – dark green). In
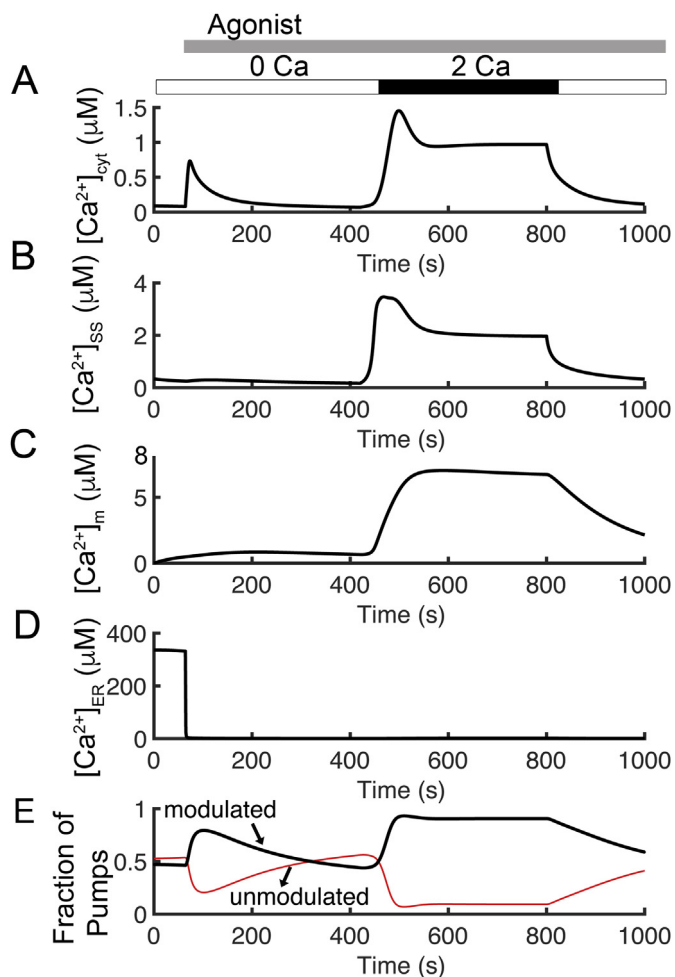
Figure 2. Simulated Ca^{2+} transients with [Ca^{2+}]$_o$ = 2.0mM from 420s to 800s and agonist application after 60s. (A) The simulated cytosolic calcium concentration. (B) Subspace calcium transients are slightly higher than the cytosolic calcium concentration. (C) Mitochondrial Ca^{2+} concentration is higher than both [Ca^{2+}]$_{cyt}$ and [Ca^{2+}]ss. (D) Initial intracellular ER store calcium concentration depletion as Ca^{2+} is released from the ER store, and an additional decrease in [Ca^{2+}]$_{ER}$ after removal of extracellular calcium. (E) A comparison of PMCA states corresponds to Ca^{2+} transient from unmodulated (red line) to modulated (black line) PMCA with [Ca^{2+}]$_o$ set to 2.0 mM from 420 s to 800 s.

the model, this is due to Ca^{2+} entry through TRPC3 during periods elevated DAG (Figure 4E and Figure 3). In experiments, TRPC3 mutants that had impaired channel function displayed smaller Ca^{2+} transients that T cells upon stimulation [52]. Experiments show that TRPC3 channels contribute to Ca^{2+} entry and are activated by membrane bound DAG [50, 51].

Mutations in CRAC channel proteins have been identified in disease. Immunodeficiency 9 is caused by mutations in the ORAI1 and Immunodeficiency 10 is caused by mutation in STIM1 [53]. Simulations show that block of ORAI1 (Ca^{2+} conductance set to zero) results greatly attenuates Ca^{2+} transient (due to block Ca^{2+} entry) and NFAT translocation to the nucleus (Figure 12AB – red). If the ER Ca^{2+} sensing function is removed, i.e.[Ca^{2+}]$_{ER}^{4.7}$ = 330 in $act_\infty = \frac{K_{act}^{4.7}}{K_{act}^{4.7}+[Ca^{2+}]_{ER}^{4.7}}$, the Ca^{2+} transient and NFAT translocation is greatly attenuated as CRAC is not activated (Figure 12AB – green). STIM1 oligomerization is considered to necessary for activation of CRAC because it thought to be a prerequisite for activation of ORAI1. In the model if the oligomerization is removed by setting the Hill coefficient to n = 1 (instead of n = 4.7) in the equation for
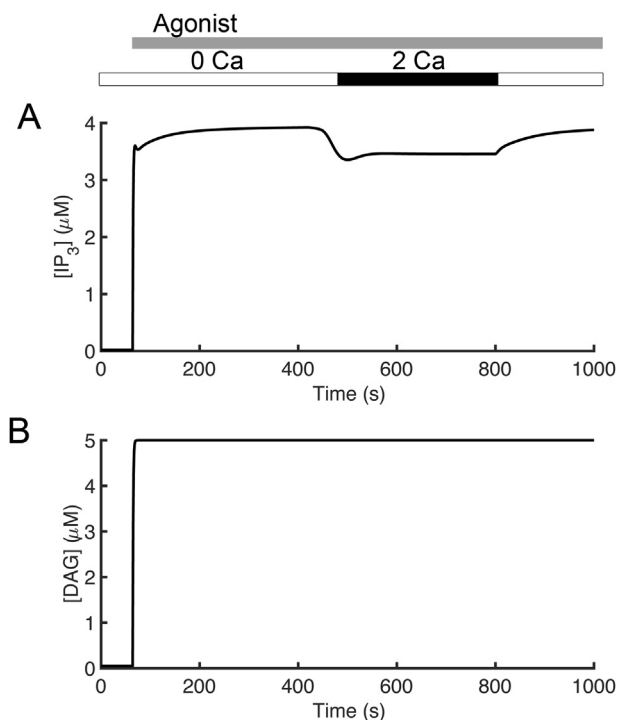

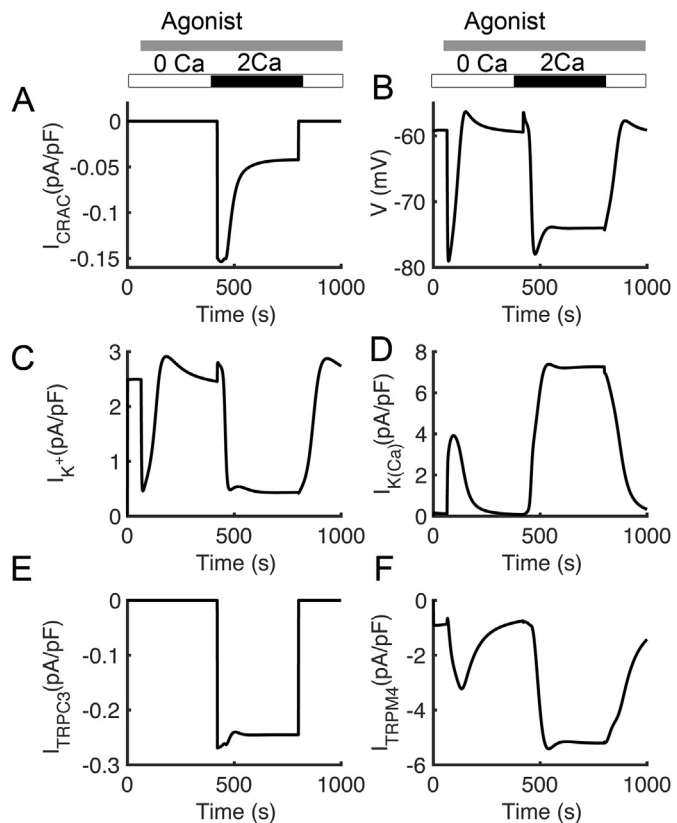Figure 3. Simulated concentrations in T cell. (A) cytosolic IP$_3$ and (B) DAG concentrations.

Figure 4. Simulated T cell membrane potential and major ionic currents. (A) Ca^{2+} release-activated Ca^{2+} (CRAC) current. (B) T cell membrane potential (C) Voltage-dependent K$^+$ current (D) Ca^{2+}-activated K$^+$ current.
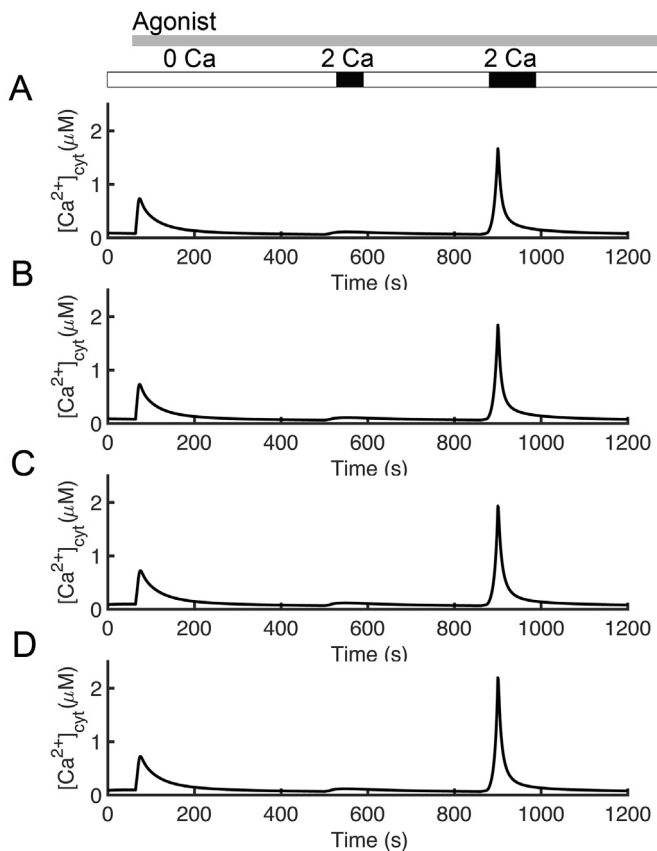
Figure 5. Simulated the effects of mitochondria, PMCA, and SERCA on intracellular calcium clearance. (A) The first spike of Ca^{2+} was due to release of Ca^{2+} from the ER resulting mainly from opening of the IP_3R, which was induced by the application of agonist. (B) The role of mitochondria is tested by blocking mitochondrial Ca^{2+} uptake. (C) The effects of the ER on Ca^{2+} clearance dynamics are determined by simulations with a disabled SERCA pump. (D) Both mitochondrial and ER uptake of Ca^{2+} are blocked by combining the protocols used in Figures. 4B and 4C.

Figure 6. Investigating the behavior of the Ca^{2+} fluxes through IP_3 receptor and CRAC channel. (A) Ca^{2+} fluxes through the IP_3 receptor from Figure 4: control (black), disabled mitochondrial Ca^{2+} uptake (red), blocked SERCA pump (green), and disabled mitochondria and SERCA (blue). (B) Ca^{2+} current for the four cases. (C) The activation of the CRAC channel is controlled by the $[Ca^{2+}]_{ER}$ for the four cases from Figure 4: control (black), disabled mitochondrial Ca^{2+} uptake (red dashed), blocked SERCA pump (green), and disabled mitochondria and SERCA (blue solid). (D) CRAC inactivation is driven by subspace Ca^{2+} concentration.

ER Ca^{2+} sensing, activation actually occurs earlier as there is a more gradual response (the Hill curve is not as steep) as seen in Figure 12AB – blue. This agrees with the idea that the oligomerization must be a part of the process of ORAI1 activation.

Experimental studies have suggested that Ca^{2+} uptake by mitochondria is necessary for CRAC activation and that in the absence of mitochondrial Ca^{2+} uptake, the CRAC channel inactivates [54]. Experiments have shown that blocking either mitochondrial calcium uptake via the Ca^{2+} uniport (J_{uni}) or blocking the mitochondrial Na^+-Ca^{2+} exchanger (J_{nc}) result in reduced Ca^{2+} entry through CRAC channels [7]. There have been various hypotheses about to the mechanism behind this phenomenon. 1) The mitochondrial uptake Ca^{2+} preventing Ca^{2+}-inactivation of CRAC [10]; 2) STIM1 oligomerization is considered to necessary for activation of CRAC. Experiments show that if mitochondrial Ca^{2+} uptake is blocked by either bock of the mitochondrial Ca^{2+} uniporter or through loss of membrane potential through uncoupling STIM1 oligomerzation is inhibited [55]. 3) Ca^{2+} bound calmodulin has been show to bind to STIM1 and ORAI1 leading to inactivation of the channel and disassociation of the STIM1 oligomer [56, 57]. 4) Block of J_{nc} results in mitochondrial Ca^{2+} overload and excess ROS production which leads to oxidation of ORAI1 inactivating Ca^{2+} entry through CRAC [58].

Model simulations were performed to explore how different mitochondrial might play a role in inactivation of the CRAC channel. Block of the mitochondrial Ca^{2+} uniporter results in a larger calcium transient (Figure 13 – red). The model suggests that this increase in Ca^{2+} due to the
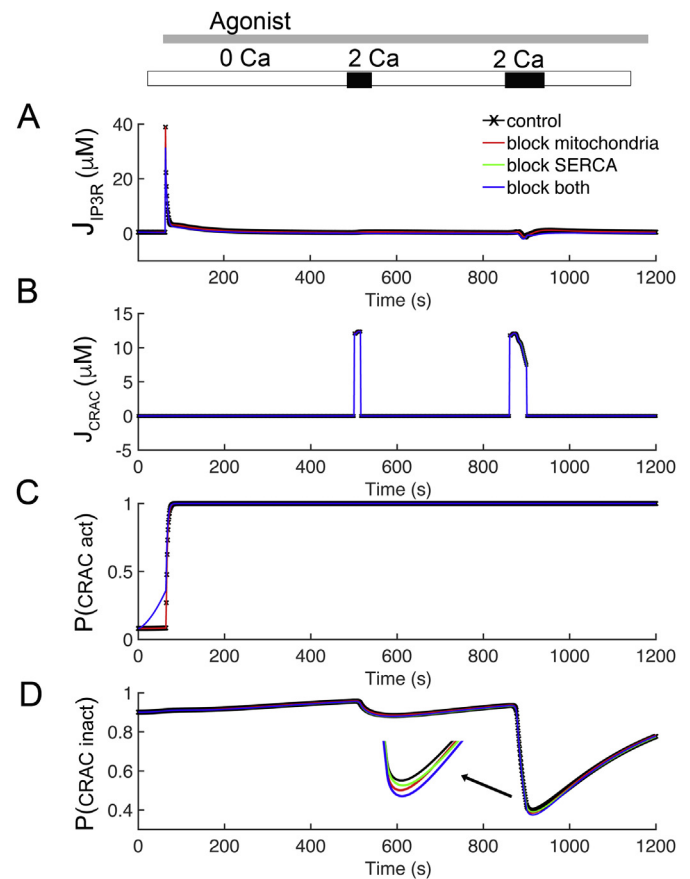
loss of the buffering of Ca^{2+} provided by the mitochondria. The CRAC channel current is inhibited over control (Figure 13C – red vs black). Blocking inactivation of the CRAC channel by Ca^{2+} results in a large increase in the Ca^{2+} channel and CRAC current suggesting that this plays a major role in controlling Ca^{2+} entry (Figure 13 – blue). In our model, this effect is assumed to be conferred by Ca^{2+} binding to CRACR2A. Calmodulin has also been shown to affect conductance through ORAI1. We modeled this effect as regulating the rate at which the channel inactivated (Figure 13 – green). This also has a large effect on CRAC current. However, none of these resulting in significant inhibition of CRAC current and loss of NFAT translocation to the nucleus. In the model all these processes to inactivate CRAC are reversible. This analysis suggests that there must be an inactivation process, not explicitly modeled from which there is slow return from the inactivated state. When such a process is included, it is possible to get mitochondrial inhibition resulting in a reduction of NFAT activation. However, such a mechanism is not presented as the mechanism is not clear.

3. Discussion

We have developed a mathematical model for calcium dynamics in T lymphocytes induced by IP_3 to mimic T cell activation by antigen. Our model includes intracellular calcium signaling dynamics, transcription factor signaling, intracellular signaling cascades, and plasma membrane
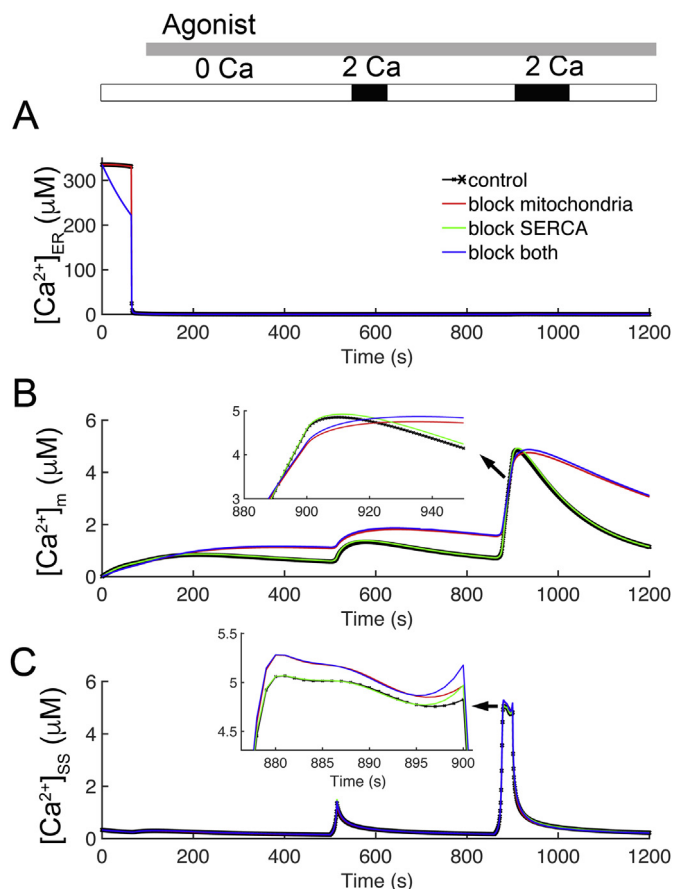
Figure 7. The model predicts the Ca^{2+} concentrations in the ER, mitochondria, and subspace. (A) The changes in ER Ca^{2+} concentration for the four cases from Figure 4: control (black), disabled mitochondrial Ca^{2+} uptake (red), blocked SERCA pump (green), and disabled mitochondria and SERCA (blue). (B) The mitochondria activity for four cases. (C) The changes in subspace Ca^{2+} concentrations for all four cases.

ion channels and pumps. The model reproduces several experimentally observed behaviors of Ca^{2+} signaling pathways in T cells. The $[Ca^{2+}]_{cyt}$ simulation results closely match the experimental data of Bautista and co-workers [26]. Calcium influx prolongs the calcium transient in the cytoplasm, and the PMCA pump plays the leading role in cytosolic Ca^{2+} clearance from the cell. This work shows that the SERCA pump and
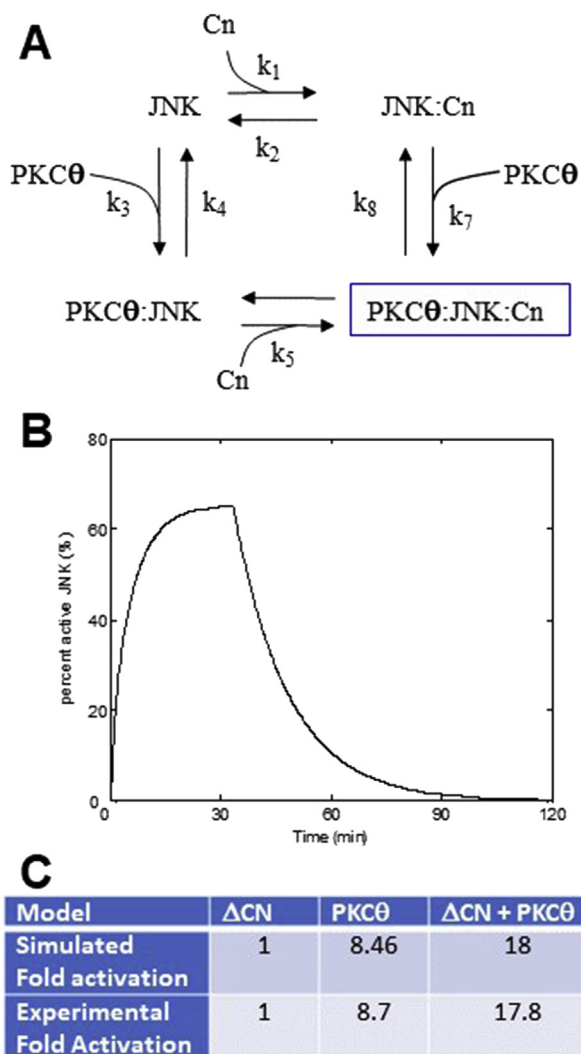
Figure 9. JNK Model. (A) Reaction dynamics of JNK. (B) Simulated JNK phosphorylation (activation). (C) Fold change of JNK phosphorylation compared to experiment (Avraham et. al., 1998 [20]).
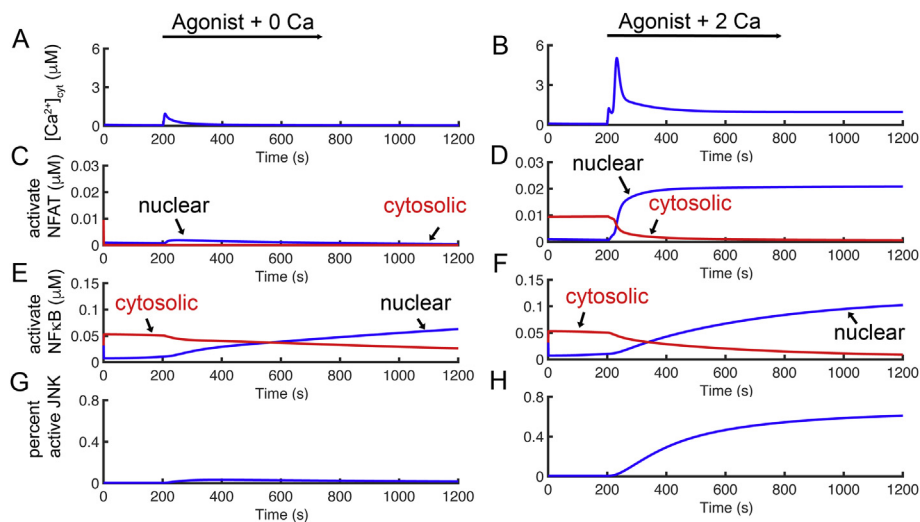

Figure 8. Transcription factors activation corresponds to the Ca^{2+} transient. (A) Transients in $[Ca^{2+}]_{cyt}$ are induced by agonist activation with 0.0 mM $[Ca^{2+}]_o$. Activation of NFAT from resting state corresponds to the top panel. (B) Simulation of Ca^{2+} transition in the cytoplasm ($[Ca^{2+}]_{cyt}$) is induced by agonist and $[Ca^{2+}]_{ot}$ was set to 2.0 mM for 1000 s. (C)–(D). Calculated active NFAT from the resting state corresponds to the Ca^{2+} transient from the top panels. (E)–(F) Simulated active NFκB from the resting state corresponds to the Ca^{2+} transient from the top panels. (G)–(H) Calculated percent active JNK from the resting state corresponds to the Ca^{2+} transient from the top panels.
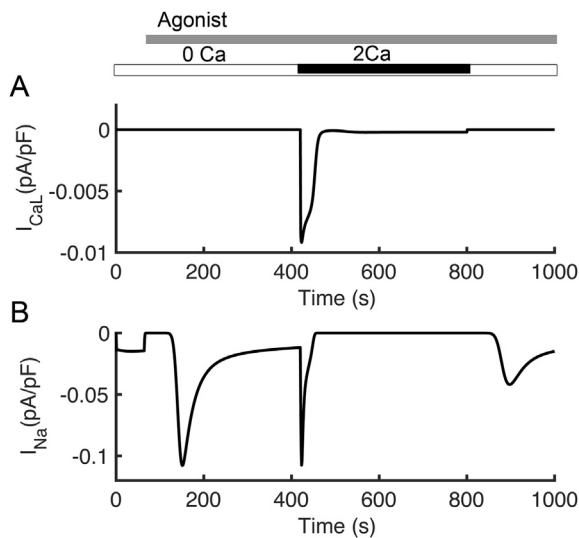
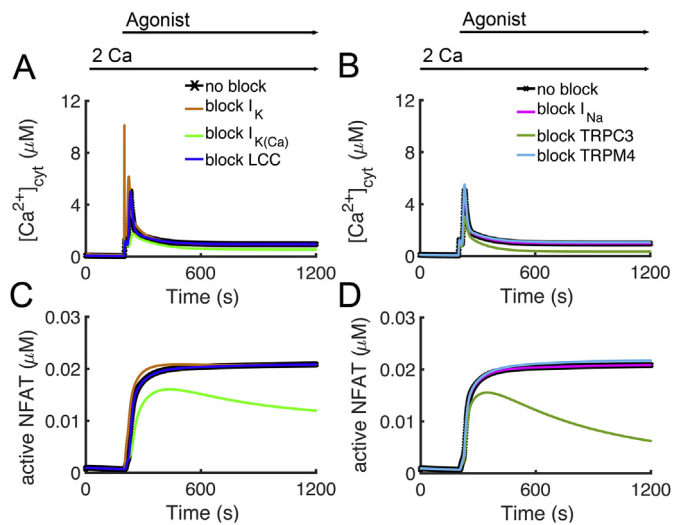**Figure 10.** Simulated T cell major ionic currents. (A) L-type Ca^{2+} current (B) Na^+ current.

Figure 11. Block of membrane currents can affect T lymphocyte activation. Agonist was applied from 200 s to 1200 s. $[Ca^{2+}]_o$ was held at 2,0 mM throughout the simulation. (A) $[Ca^{2+}]_{cyt}$ transients are reduced with block of $I_{K(Ca)}$ (green) compared to control (black). Under the current channel expression levels, block of I_{CaL} (blue) and I_K (tan) have little effect on the $[Ca^{2+}]_{cyt}$ transient. (C) NFAT translocation to the nucleus is attenuated with block of $I_{K(Ca)}$ (green) compared to control (black). Block of I_{CaL} (blue) and I_K (tan) have only a small effect on NFAT translocation to the nucleus. (B) $[Ca^{2+}]_{cyt}$ transients are reduced with block of I_{TRPC3} (dark green) compared to control (black). Under the current channel expression levels, block of I_{TRPM4} (light blue) and I_{Na} (fuschia) have little effect on the $[Ca^{2+}]_{cyt}$ transient. Note that increasing I_{TRPM4} decreases the $[Ca^{2+}]_{cyt}$ transient. (D) NFAT translocation to the nucleus is attenuated with block of I_{TRPC3} (dark green) compared to control (black). Block of I_{Na} (light blue) and I_{TRPM4} (fuchsia) have only a small effect on NFAT translocation to the nucleus.

Figure 12. Blocking STIM1 and ORAI greatly attenuate T lymphocyte activation. Agonist was applied from 200 s to 1200 s. $[Ca^{2+}]_o$ was held at 2,0 mM throughout the simulation. (A) Block of the channel conductance of ORAI1 (red) or blocking the Ca^{2+} sensitivity of STIM1 (green) greatly attenuate the $[Ca^{2+}]_{cyt}$ transient compared to control (black). Blocking the cooperativity of STIM1 (blue) but still allowing monomers to activate ORAI1 has little effect the $[Ca^{2+}]_{cyt}$ transient. (B) Block of the channel conductance of ORAI1 (red) or blocking the Ca^{2+} sensitivity of STIM1 (green) greatly attenuate NFAT translocation to the nucleus compared to control (black). Blocking the cooperativity of STIM1 (blue) but still allowing monomers to activate ORAI1 has little effect on NFAT translocation to the nucleus.

mitochondria together have an impact on the rate of Ca^{2+} extrusion. The model also explores the contributions of mitochondria dynamics and I_{CRAC} to activation of NFAT. Experimental studies indicated that mitochondria localized close to the cell membrane absorb calcium from I_{CRAC} [9, 10], suggesting that increases in local $[Ca^{2+}]_{cyt}$ leads to inactivation of I_{CRAC}. The model explores this hypothesis and assumes a local subspace contains mitochondria near the CRAC channel. In order to further validate the predictive value of the model, simulation results are compared to
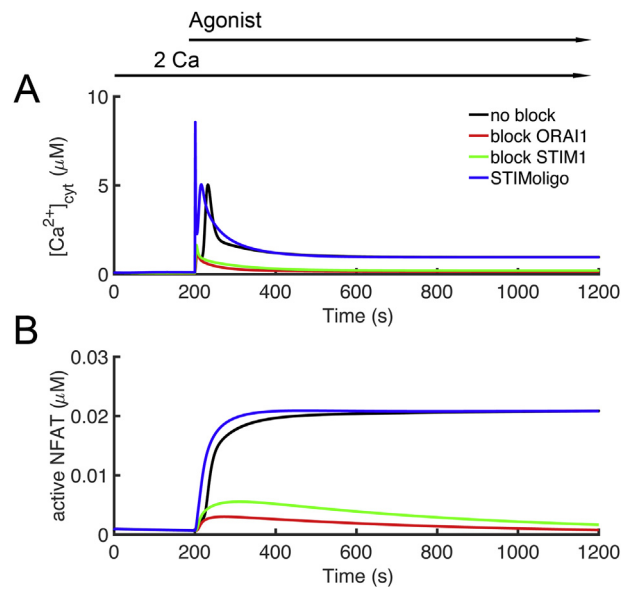
experimental data that was not used to constrain the model. In particular, the time course of $[Ca^{2+}]_{SS}$ and $[Ca^{2+}]_m$ from Figure 2B, C compares well to the experimental data. The significant rise in $[Ca^{2+}]_m$ close to the site of Ca^{2+} entry is similar to that shown in Schwindling et al (2010) [59]. The model predictions about $[Ca^{2+}]_{SS}$ and plasmalemmal Ca^{2+} ATPase currents are similar to the experimental results of Quintana et al 2011 [60].

We have also tested the role of the voltage-dependent sodium (Nav1.5) that is only present in a small fraction of cells [61]. To this end, a voltage-dependent sodium channels based on the experimentally verified Luo-Rudy model [32] was also included to test its possible role in T cell activation. The currents generated by this channel were small and sensitivity analysis showed no significant effect of Na^+ channel conductance on NFAT translocation into the nucleus.

In this paper, our simulations suggest that NFAT and NFκB activation can be inhibited by decreasing $[Ca^{2+}]_{cyt}$ through termination of Ca^{2+} release from the ER and thus preventing opening of CRAC channels. This finding suggests that blocking I_{CRAC} might be a possible target for immunosuppression. The exact mechanism of opening of CRAC channels is still not clear. One hypothesis is that ER stores reside close to CRAC channels [9] and there is some sort of physical sensor that transmits ER depletion to the CRAC channel. Many studies showed that Ca^{2+} influx has a great impact on T-cell activation and proliferation [9, 33]. Our model suggests that Ca^{2+} entry from CRAC channels is essential for NFAT and NFκB activity. The model can also be used to understand other mutations leading to T lymphocyte dysfunction. Mutations in the Gimap5 gene lead the immune system disorders through T cell dysfunction [62]. Gimap5 inhibits a protein that inactivates GSK3, there the mutation leads to increased GSK3 activity [62]. Our previous studies have shown that GSK3 dephosphorylates nuclear NFAT allowing it to be translocated out of the nucleus [63]. The model predicts that the Gimap5 mutation might lead to immune dysfunction by increasing NFAT export from the nucleus. Mutations in the IP$_3$R can lead to T cell lymphoma with some mutants
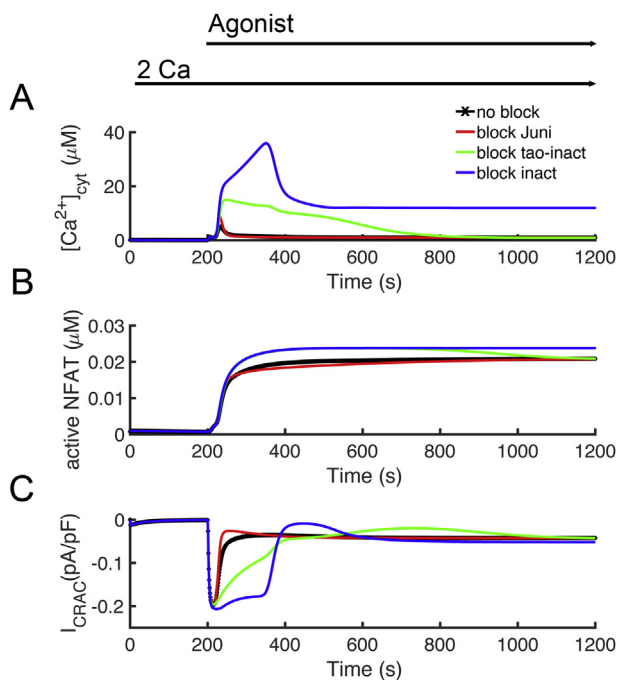
Figure 13. The role of mitochondrial Ca^{2+} uptake on T lymphocyte activation. Agonist was applied from 200 s to 1200 s. [Ca^{2+}]$_o$ was held at 2,0 mM throughout the simulation. (A) Block of the channel conductance of the mitochondrial Ca^{2+} uniporter (red) slightly increases the [Ca^{2+}]$_{cyt}$ transient compared to control (black). Blocking the Ca^{2+}-dependent inhibition of ORAI1 (blue) or blocking the Ca^{2+}-dependent rate of inhibition (green) result in a large [Ca^{2+}]$_{cyt}$ transient. (B) Block of the channel conductance of the mitochondrial Ca^{2+} uniporter (red) slightly decreases NFAT translocation to the nucleus compared to control (black). Blocking the Ca^{2+}-dependent inhibition of ORAI1 (blue) or blocking the Ca^{2+}-dependent rate of inhibition (green) increases NFAT translocation to the nucleus. (C) Block of the channel conductance of the mitochondrial Ca^{2+} uniporter (red) slightly decreases CRAC current compared to control (black). Blocking the Ca^{2+}-dependent inhibition of ORAI1 (blue) or blocking the Ca^{2+}-dependent rate of inhibition (green) result in increased CRAC current.

contributing to increased IP$_3$R Ca^{2+} release while others lead to increased IP$_3$ sensitivity with no observed change to Ca^{2+} dynamics [64]. Our previous work in Ca^{2+} dynamics in cardiac myocytes offers and explanation [65, 66]. With increased IP$_3$R open probability, there is Ca^{2+} efflux (leak) from the ER. This results in lower ER Ca^{2+} content reducing the driving force for Ca^{2+} efflux during IP$_3$R opening. The production of increased open probability and decreased driving force returns the Ca^{2+} transient to normal levels.

Our model successfully simulates the calcium dynamics and control of NFAT and NFκB activation. However, not every feature present in the T cell could be represented, only selected ones. There are many improvements to the model possible to address important scientific questions, including upstream elements of the signaling pathway, the role mitochondrial function, cytoskeleton, spatial reorganization, and changes in gene expression play in T cell physiology.

Upstream elements of the T cell activation signaling pathway can be added to the model, for example, the activation of DAG and protein kinase C (PKC) on calcium and its feedback on phospholipase C (PLC). The early events in T cell activation show that IP$_3$ induction of Ca^{2+} release from ER stores follows the cleavage of PIP$_2$ by PLCγ1, and suggest that this time delay in the activation of PLCγ1 could account for the experimentally observed a delay in calcium signaling [67].

Calcium signaling between the mitochondria and ER plays a role in T cell physiological processes such as activation, effector functions, lineage determination, apoptosis, autophagy and mitochondrial bioenergetics

[68, 69, 70, 71]. It has been suggest that mitochondrial contact sites are necessary for the reprogramming and stimulation of energy metabolism that occurs during T cell activation [69]. In its current form, the model cannot address these issues. We understand that the role mitochondria play in T cell activation is topic of current research and hope to include that in future work. We have a detailed model of ionic homeostasis and energy metabolism that we developed for the cardiac myocyte that demonstrates activation of energy metabolism. It is clear that increases in mitochondrial Ca^{2+} can stimulate energy production, but changes in ADP, ATP, and NADH levels can also contribute to meeting the increased energy demands during T cell activation. There is also experimental evidence that NFAT activation triggers signaling cascades that also increase energy production in the T cell [14]. The model currently does not address these issues, but lays the foundations for future modeling. This model described membrane ion channels, calcium dynamics and transcription factor signaling during T cell activation. While we have not modeled apoptosis, and autophagy, there are models that have been developed to describe these processes that might be adapted for this purpose. In future work, we hope to add features to this model for the T cell and explore these issues.

The changes to spatial organization, membrane ultrastucture, and signaling pathways and changes to gene expression are crucial to T cell activation and other physiological processes [72, 73]. This suggests that the development of a spatial model might be helpful in understanding T cell physiology. For example, the STIM1:ORAI1 puncti that form during T cell activation display single channel ORAI responses with complex dynamics. Describing these might require development of a spatial stochastic model [74]. Different types of T cells have different ion channel expression. The model in the future could be used to explore these cell-to-cell differences.

NFAT activation resulting from Ca^{2+} mobilization is important for the differentiation into T helper 1 (Th1), Th2, Th17, regulatory T (Treg), and follicular helper T cells (Tfh) through interaction with different other transcription factors such as GATA3 and Foxp3 [75]. Another future question that can be addressed by the model is the differentiation of T cells after activation requires activation of different transcription factors. This might arise different patterns of signaling that might arise from cell heterogeneity.

During T cell activation there is a reorganization of cellular structure to form the immunological synapse [76]. These changes rely on the microtubular network and actin cytoskeleton. Movement of the cytoskeleton responds to Ca^{2+} mobilization [72]. There has been significant computational modeling studies on how the cytoskeleton reorganizes cell structure, for example, in dendritic spines, that can be used in future work to understand these dynamics [77].

4. Materials and methods

4.1. The model

The De Young-Keizer model [78] was revised to include four different Ca^{2+} compartments, the ER, the cytosol, the mitochondria, and a subspace between the plasma membrane and mitochondria. The model describes the membrane potential and several ion channels that regulate it. The model also includes the Ca^{2+} release-activated Ca^{2+} (CRAC) channel (STIM1, ORAI1, and CRACR2A), the plasmalemmal Ca^{2+}-ATPase (PMCA), and the dynamics of IP$_3$ production and degradation. The model consists differential equations describing the time rate of change of the following quantities: (1) the ER Ca^{2+} concentration ([Ca^{2+}]$_{ER}$); (2) the cytosolic IP$_3$ concentration ([IP$_3$]$_{cyt}$); (3) the eight states of IP$_3$R gating; (4) the mitochondrial Ca^{2+} concentration ([Ca^{2+}]$_m$); (5) the subspace Ca^{2+} concentration ([Ca^{2+}]$_{SS}$); (6) the fraction of PMCA channels in the unmodulated state (u); (7) the cytosolic Ca^{2+} concentration ([Ca^{2+}]$_{cyt}$); (8) the three gates of the sodium channel (I$_{Na}$); (9) the voltage dependent K$^+$ channel (I$_K$); (10) the calcium activated potassium channel I$_{K(Ca)}$; (11) the L-type Ca^{2+} current; (12) the TRPM4 current (I$_{TRPM4}$); (13) the

TRPC3 current (I_{TRPC3}); (14) the membrane potential (V). The parameter values and definitions are given in Tables 1, 2, 3, 4, 5, 6, 7, 8, and 9. Changes to the parameters for a particular simulation are stated in the text where the simulations are described. Model Fortran code is included as supplementary material. Sensitivity analysis was also performed to ensure that the model was not overly sensitive to any model parameters (Figure 14).

The ER store dynamics are governed by four processes: (1) Ca^{2+} buffering (β_{ER}), (2) Ca^{2+} sequestration in the ER though the sarcoplasmic reticulum calcium ATPase (J_{SERCA}) from the cytosol, and (3) Ca^{2+} release from the ER through the IP_3 receptor (J_{IP3R}). The balance equation for $[Ca^{2+}]_{ER}$ is

$$\frac{d[Ca^{2+}]_{ER}}{dt} = \beta_{ER}\left(\frac{J_{SERCA} - J_{IP_3R}}{V_{ER}/V_{cyt}}\right) \tag{1}$$

where β_{ER} represents the fractional buffering of Ca^{2+} in the ER using the rapid buffering approximation developed by Wagner and Keizer [79] described as follows:

$$\beta_{ER} = \left\{1 + \frac{[B_S^{ER}]_{ER}K_S^{ER}}{(K_S^{ER} + [Ca^{2+}]_{ER})^2} + \frac{[B_e^{ER}]K_e^{ER}}{(K_e^{ER} + [Ca^{2+}]_{ER})^2}\right\}^{-1} \tag{2}$$

where $[B_S^{ER}]_{ER}$ is the total concentration of stationary buffer in the ER, and other rate constants are defined as shown in Table 3.

The SERCA flux for Ca^{2+} movement from the cytoplasm into the ER, (J_{SERCA}) is described by

$$J_{SERCA} = \frac{v_{SERCA}[Ca^{3+}]_{ER}^2}{[Ca^{3+}]_{ER}^2 + K_{SERCA}^2} \tag{3}$$

where K_{SERCA} is the binding constant for Ca^{2+} to the pump.

The flux of Ca^{2+} through the IP_3 receptor (J_{IP3R}) into the cytosol can be described by

$$J_{IP_3R} = \frac{V_{ER}}{V_{cyt}}v_1X_{110}^3\left([Ca^{2+}]_{ER} - [Ca^{2+}]_{cyt}\right) \tag{4}$$

where v_1 is the maximal Ca^{2+} flux rate through the IP_3R, and X_{110} is the fraction of IP_3R subunits in the open state. The ER and cytosolic Ca^{2+} concentrations are represented by $[Ca^{2+}]_{ER}$ and $[Ca^{2+}]_{cyt}$, respectively, and their difference describes the Ca^{2+} concentration gradient.

The notation X_{110} comes from the model of the IP_3 receptor developed by De Young and Keizer and denotes that IP_3 has already bound a channel subunit (1 in the first subscript position), but activating Ca^{2+} is bound (1 in the second subscript position) but no inactivating Ca^{2+} is bound (0 in the third subscript position has yet bound so the channel is open) (Figure 1C) [78]. The channel state X_{110} is cubed to fit the experimental data and suggests that three subunits must be in this state for the channel to conduct Ca^{2+}. The rate constants are defined as shown in Table 2. The equations for activation and inactivation states of cytosolic IP_3 receptors by Ca^{2+} are describing in the following equations:

Table 9. JNK activation rate constants.

Rate Constant	Value
k_1	0.016
k_2	0.00038
k_3	0.00012
k_4	0.0075
k_5	0.00001
k_6	0.00088
k_7	0.00001
k_8	0.00025

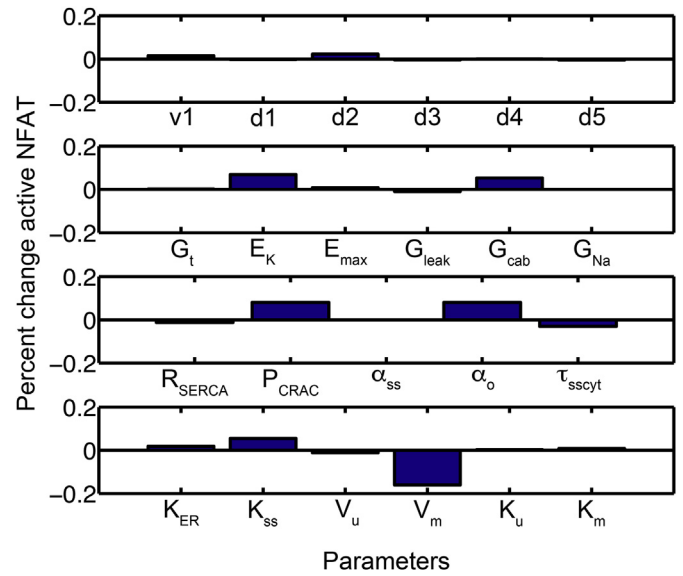**Figure 14.** Sensitivity analysis for NFAT activation depended upon model parameters.

$$f_1 = b_5X_{010} - a_5[Ca^{2+}]_{cyt}X_{000} \tag{5}$$

$$f_2 = b_1X_{100} - a_1[IP_3]_{cyt}X_{000} \tag{6}$$

$$f_3 = b_4X_{001} - a_4[Ca^{2+}]_{cyt}X_{000} \tag{7}$$

$$f_4 = b_5X_{110} - a_5[Ca^{2+}]_{cyt}X_{100} \tag{8}$$

$$f_5 = b_2X_{101} - a_2[Ca^{2+}]_{cyt}X_{100} \tag{9}$$

$$f_6 = b_1X_{110} - a_2[IP_3]_{cyt}X_{010} \tag{10}$$

$$f_7 = b_4X_{011} - a_4[Ca^{2+}]_{cyt}X_{010} \tag{11}$$

$$f_8 = b_5X_{011} - a_5[Ca^{2+}]_{cyt}X_{001} \tag{12}$$

$$f_9 = b_3X_{101} - a_3[IP_3]_{cyt}X_{001} \tag{13}$$

$$f_{10} = b_2X_{111} - a_2[Ca^{2+}]_{cyt}X_{110} \tag{14}$$

$$f_{11} = b_5X_{111} - a_5[Ca^{2+}]_{cyt}X_{101} \tag{15}$$

$$f_{12} = b_3X_{111} - a_3[IP_3]_{cyt}X_{011} \tag{16}$$

$$\frac{dX_{000}}{dt} = f_1 + f_2 + f_3 \tag{17}$$

$$\frac{dX_{100}}{dt} = f_4 + f_5 - f_2 \tag{18}$$

$$\frac{dX_{010}}{dt} = -f_1 + f_6 + f_7 \tag{19}$$

$$\frac{dX_{001}}{dt} = f_8 - f_3 + f_9 \tag{20}$$

$$\frac{dX_{110}}{dt} = -f_4 - f_6 + f_{10} \tag{21}$$

$$\frac{dX_{101}}{dt} = f_{11} - f_9 - f_5 \tag{22}$$

$$\frac{dX_{011}}{dt} = -f_8 - f_7 + f_{12} \tag{23}$$

$$\frac{dX_{111}}{dt} = -f_{11} - f_{12} - f_{10} \tag{24}$$

The IP$_3$ production and degradation dynamics in the cytosol are based on the Swillens-Mercan model [27]. The equation of free cytosolic concentration of IP$_3$ ([IP$_3$]$_{cyt}$) is given by

$$\frac{d[IP_3]_{cyt}}{dt} = v_4 - \frac{v_5}{\left[1 + \left(\frac{K_5}{[IP_3]_{cyt}}\right)^h\right]} - \frac{v_6}{\left[1 + \left(\frac{K_6}{[IP_3]_{cyt}}\right)^h\right]}\frac{1}{\left[1 + \left(\frac{K_7}{[Ca^{2+}]_{cyt}}\right)\right]} \tag{25}$$

where v_4 is the rate of formation of IP$_3$ from phosphatidyl inositol (PIP$_2$) by phospholipase C (PLC). In the second term, v_5 is the maximal rate of dephosphorylation of IP$_3$ by a 5-phosphatase governed by the binding constant K_5. The third term represents the rate of IP$_3$ phosphorylation to inositol 1,3,4,5-tetrakisphosphate by a 3-kinase with maximal rate v_6 and binding constant K_6 that is increased by Ca^{2+} with binding constant K_7 (Figure 1B) [27]. The rate constants are defined as shown in Table 1.

The production dynamics for diacyl glycerol (DAG) is that same as IP$_3$ as they are both produced by PLC. The dynamics equation of free cytosolic concentration of DAG is

$$\frac{d[DAG]_{cyt}}{dt} = v_4 - v_8[DAG]_{cyt} \tag{26}$$

The mitochondrial Ca^{2+} dynamics are governed by three processes: (1) Ca^{2+} influx through the Ca^{2+} uniporter (J$_{UNI}$), (2) Ca^{2+} efflux through the Na$^+$-Ca^{2+} exchanger (J$_{NCLX}$) and (3) Ca^{2+} buffering [80, 81]. The Ca^{2+} influx through uniporter (J$_{UNI}$) is described as by Nguyen and Jafri [81] using on the Goldman-Hodgkin-Katz (GHK) equation as follows

$$J_{UNI} = P_{UNI}\frac{z\Psi_m F}{V_{mito}RT}\frac{\alpha_m[Ca^{2+}]_m \exp\left[\frac{-z\Psi_m F}{RT}\right] - \alpha_{SS}[Ca^{2+}]_{ss}}{\exp\left[\frac{-z\Psi_m F}{RT}\right] - 1} \tag{27}$$

where P_{UNI} is the permeability of the uniporter, z is the valence of Ca^{2+}, Ψ_m is the mitochondrial membrane potential, F is Faraday's constant, V_{mito} is the mitochondrial matrix volume, R is the ideal gas constant, T is the absolute temperature, α_m and α_{SS} are the mitochondrial and subspace activity coefficients for Ca^{2+} at the mouth of the uniporter which is thought to be a channel. The Ca^{2+} efflux through the Na$^+$-Ca^{2+} exchanger (J$_{NC}$) used the formulation by Jafri and Nguyen [81] described by

$$J_{NC} = \frac{v_{NC}\left[e^{0.5\Psi_m F/RT}\frac{[Na^+]_{ss}^3[Ca^{2+}]_m}{K_{Na}^3 K_{Ca}} - e^{-0.5\Psi_m F/RT}\frac{[Na^+]_m^3[Ca^{2+}]_{ss}}{K_{Na}^3 K_{Ca}}\right]}{1 + \frac{[Na^+]_{ss}^3}{K_{Na}^3} + \frac{[Ca^{2+}]_m}{K_{Ca}} + \frac{[Na^+]_{ss}^3[Ca^{2+}]_m}{K_{Na}^3 K_{Ca}} + \frac{[Na^+]_m^3}{K_{Na}^3} + \frac{[Ca^{2+}]_{ss}}{K_{Ca}} + \frac{[Na^+]_m^3[Ca^{2+}]_{ss}}{K_{Na}^3 K_{Ca}}} \tag{28}$$

where K_{Na} is the Na$^+$ binding constant, K_{Ca} is the Ca^{2+} binding constant, V_{NC} is the maximal exchanger velocity, [Na$^+$]$_{ss}$ is the subspace Na$^+$ concentration, and [Na$^+$]$_m$ is the mitochondrial Na$^+$ concentration (Table 4). These two fluxes comprise the balance equations for [Ca^{2+}]$_m$

$$\frac{d[Ca^{2+}]_m}{dt} = \beta_{Ca}(J_{UNI} - J_{NC}) \tag{29}$$

where β_{Ca} is a constant describing Ca^{2+} buffers in the mitochondria.

Mitochondrial Ca^{2+} uptake dynamics and depletion of the endoplasmic reticulum (ER) trigger prolonged Ca^{2+} influx through CRAC channels [9, 10, 26, 33, 74]. The Ca^{2+} influx through CRAC channels (J$_{CRAC}$) can be described by contributions from three components STIM1, CRACR2A, calmodulin and ORAI1 [82,83]. STIM1 oligomerizes to activate the channel when [Ca^{2+}]$_{ER}$ is depleted and can be described by the Hodgkin-Huxley formalism

$$\frac{dact}{dt} = \frac{act_\infty - act}{\tau_{bb}} \tag{30}$$

where *act* is the fraction of channels activated, τ_{bb} is the time constant, and the steady state probability of the activation gate is

$$act_\infty = \frac{K_{act}^{4.7}}{K_{act}^{4.7} + [Ca^{2+}]_{ER}^{4.7}} \tag{31}$$

with K_{act} as the Ca^{2+} dissociation constant [84, 85]. CRAC2A binding to ORAI1 is required for proper Ca^{2+} signaling during T-cell activation [83, 86]. CRACR2A disassociates from the ORAI1 protein when it binds Ca^{2+} leading to inactivation of the channel [87]. Binding of Ca^{2+}/calmodulin to ORAI1 has also been shown to inactivate the channel Ca^{2+} bound [56, 57]. This inactivation process is described by

$$\frac{dinact}{dt} = \frac{inact_\infty - inact}{\tau_{cc}} \tag{32}$$

where *inact* is the fraction of channels activated. The time constant

$$\tau_{cc} = \frac{200k_{cc}^2}{K_{cc}^2 + [Ca^{2+}]_{SS}^2} \tag{33}$$

represents the inhibitory action of Ca^{2+}/calmodulin with K_{cc} as the calcium binding affinity. The steady-state probability the inactivation gate

$$inact_\infty = \frac{K_{inact}}{K_{inact} + [Ca^{2+}]_{SS}} \tag{34}$$

with K_{inact} as the dissociation constant for Ca^{2+} binding represents Ca^{2+} binding to CRACR2A. These are approximations as quantitative data is not yet available. The I$_{CRAC}$ is based on the GHK equation and closely matches the experimental results shown by Bautista et. al., [26], (Figure 15A).

$$I_{CRAC} = P_{CRAC}\frac{z^2 VF^2}{RT}\frac{\alpha_{SS}[Ca^{2+}]_{ss}\exp\left[\frac{zVF}{RT}\right] - \alpha_o[Ca^{2+}]_o}{\exp\left[\frac{zVF}{RT}\right] - 1} \tag{35}$$

here P_{CRAC} is the permeability of Ca^{2+}, V is the cell membrane potential, and α_o is the extracellular activity coefficient for Ca^{2+} at the mouth of the channel. In this context, α_{SS} is the subspace activity coefficient at the mouth of the I$_{CRAC}$ channel. The rate constants are shown in Table 5. Finally, the Ca^{2+} is

$$J_{CRAC} = \frac{I_{CRAC}}{2FV_{SS}} \times act \times inact \tag{36}$$

where V_{SS} is subspace volume.

The final flux that influences the Ca^{2+} dynamics is the transfer from the subspace into the cytosol (J$_{SScyt}$)

$$J_{SScyt} = \frac{[Ca^{2+}]_{SS} - [Ca^{2+}]_{cyt}}{\tau_{SScyt}} \tag{37}$$

where τ_{sscyt} is transfer time between the subspace and the cytosol. The subspace Ca^{2+} dynamics can be described in terms of the fluxes described above by

$$\frac{d[Ca^{2+}]_{SS}}{dt} = \beta_{ss}\left(\frac{V_{mito}}{V_{SS}}(J_{NC} - J_{UNI}) + \frac{V_{cyt}}{V_{SS}}(J_{CRAC} - J_{SScyt})\right) \tag{38}$$

where V_{cyt} is the cytosolic volume and the volume ratios rescale the fluxes to account for the volume difference between the subspace and the other compartments (Table 6). The factor β_{ss} represents the buffering in the subspace and is described by

$$\beta_{ss} = \left\{1 + \frac{[B_s]_{ss}K_s^{cyt}}{Ca^{2+}][Ca^{2+}][Ca^{2+}]_{ss})^2} + \frac{[B_e]_{ss}K_e^{ss}}{Ca^{2+}][Ca^{2+}][Ca^{2+}]_{ss})^2}\right\}^{-1} \tag{39}$$

The total concentrations of stationary (s) and exogenous (e) buffers are represented by $[B_j]_{SS}$, and $K_j^{ss}(j = s,e)$ are their dissociation constants for Ca^{2+} (Table 3).

According to Bautista and co-workers, the plasma-membrane Ca^{2+}-ATPase (PMCA) controls a majority of the extrusion of Ca^{2+} and is slowly modulated by changes in calcium concentration [26]. They observed altered Michaelis-Menten kinetics that describes Ca^{2+} removal in the modulated (pre-incubated with high Ca^{2+}) and unmodulated states. A Hodgkin-Huxley type formalism is used here to describe transitions between the two states of PMCA designated U (unmodulated) and M (modulated) (M) PMCA. Transitions to and from the modulated state are represented by the rate constants w_1 which depends upon $[Ca^{2+}]_{cyt}$ and w_2,

$$U \underset{w_2}{\overset{w_1}{\rightleftharpoons}} M \tag{40}$$

where

$$w_1(Ca^{2+}) = p_1 \times [Ca^{2+}]_{cyt} \tag{41}$$

and $w_2 = 0.01$, where $p_1 = 0.1\ \mu M^{-1}$ is the rate constant for activation of the PMCA. These rate constants were estimated to match experimental results. The fraction of the pumps in the unmodulated state (u) can be described by

$$\frac{du}{dt} = \frac{u_\infty - u}{\tau_u} \tag{42}$$

where

$$\tau_u = \frac{1}{w_1(Ca^{2+}) + w_2} \tag{43}$$

and

$$u_\infty = \frac{w_2}{w_1(Ca^{2+}) + w_2} \tag{44}$$

The total PMCA (plasma membrane Ca^{2+}-ATPases) flux (J_{PMCA}), including contributions from both the unmodulated and modulated states, is given by

$$J_{PMCA} = \left(u\frac{v_u[Ca^{2+}]_{cyt}^{1.8}}{K_u^{1.8} + [Ca^{2+}]_{cyt}^{1.8}} + m\frac{v_m[Ca^{2+}]_{cyt}^{2.1}}{K_m^{2.1} + [Ca^{2+}]_{cyt}^{2.1}}\right) \tag{45}$$

where m is the fraction of pumps in the modulated state (m + u = 1). The parameters v_u and v_m denote the maximal rate of unmodulated and modulated PMCA fluxes, and K_u and K_m are the $[Ca^{2+}]_{cyt}$ for half maximal velocity for V_u and V_m, respectively. These parameters, including the exponents 1.8 and 2.1, are taken to fit the experimental data observed by Bautista and coworkers [26]. Figure 15B shows the changes in J_{PMCA} as a function of $[Ca^{2+}]_{cyt}$ during unmodulated and modulated PMCA. PMCA efflux increases when $[Ca^{2+}]_{cyt}$ increases more in the modulated state (Figure 15B − red line) than in the unmodulated state (Figure 15B − blue line), which are fitted to experimental data of Bautista and co-workers [26].

I_{PMCA} is the total PMCA current is given by

$$I_{PMCA} = J_{PMCA}\left(V_{cyt} \times z \times F \times 10^6\right) \tag{46}$$

The balance equation for cytosolic calcium concentration is given by

$$\frac{d[Ca^{2+}]_{cyt}}{dt} = \beta_{cyt}\left(J_{IP_3R} - J_{SERCA} - J_{PMCA} + J_{SScyt} + J_{CaL} + J_{TRPC3}\right) \tag{47}$$

using fluxes described above. In this equation, β_{cyt} is the cytosolic Ca^{2+} buffering factor,

$$\beta_{cyt} = \left\{1 + \frac{[B_s]_{cyt}K_s^{cyt}}{\left(K_s^{cyt} + [Ca^{2+}]_{cyt}\right)^2} + \frac{[B_e]_{cyt}K_e^{cyt}}{\left(K_e^{cyt} + [Ca^{2+}]_{cyt}\right)^2}\right\}^{-1} \tag{48}$$

with the total concentrations of stationary (s) and exogenous (e) buffers represented by $[B_j]_{cyt}$, and $K_j^{cyt}(j = s,e)$ their dissociation constants for Ca^{2+}. Note that the model assumes that the total buffer concentrations in the subspace and cytosol are equal (Table 3).

The equations of model I_K current are defined as follows

$$I_K = G_t \times xn \times xj \times (V - E_K) \tag{49}$$

the activation (xn) and inactivation (xj) gating variables are fitted to experimental data of Dupuis and co-workers [28] as shown in Figure 16 and described by the equations

$$xn_\infty = \frac{1}{1 + e^{(V+11)/-15.2}} \tag{50}$$

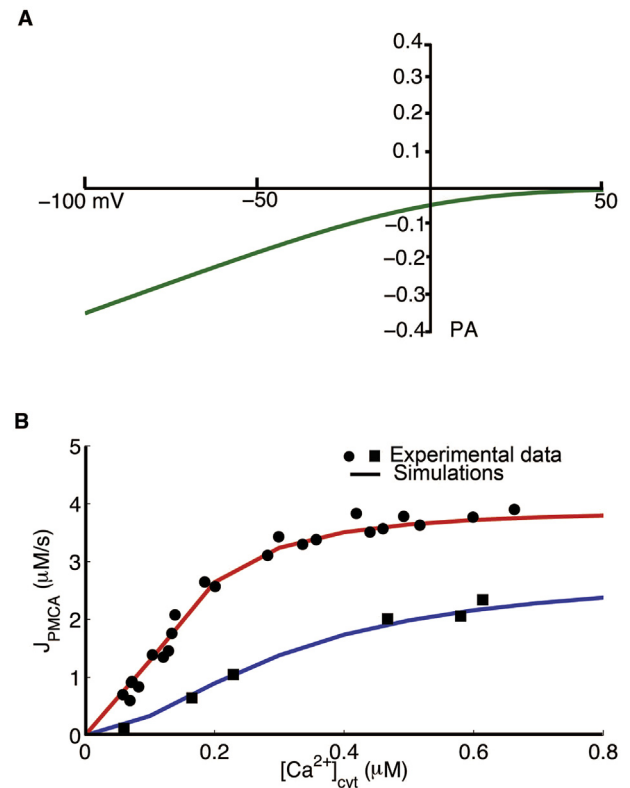$$xj_\infty = \frac{1}{1 + e^{(V+45)/9}} \tag{51}$$

A

B

Figure 15. Simulated I_{CRAC} and J_{PMCA}. (A) Extracellular calcium concentration was set to 2.0 mM to measure I_{CRAC} from -100 mV to +50 mV. (B) J_{PMCA} as function of $[Ca^{2+}]_{cyt}$ is shown for two pump states, modulated and unmodulated.

$$\tau_{xn} = \frac{1}{(0.2e^{0.032(V-0.0677)})} \tag{52}$$

and

$$\tau_{xj} = \frac{15}{0.03(e^{0.0083(V+40.8)} + 0.4865e^{-0.06(V+60.49)})} \tag{53}$$

The $I_{K(Ca)}$ current can be described by

$$I_{K(Ca)} = \frac{E_{max}}{1 + \left(\frac{K_d}{[Ca^{2+}]_{cyt}}\right)^3} \times (V - E_K) \tag{54}$$

where $E_{max} = 0.8$ nS [6] and $K_d = 0.45$ μM is derived from the experiments of Verheugen and co-workers [29].

The model of the fast Na^+ current include activation and inactivation gate is based on the Luo-Rudy model [32]. The formulation is given by

$$I_{Na} = G_{Na} \times m^3 \times h \times j \times (V - E_{Na}) \tag{55}$$

Activation gate m and inactivation gate are described as
For V≥-40 mV

$$\alpha_h = \alpha_j = 0.0 \tag{56}$$

$$\beta_h = \frac{1}{0.13 \times (1 + e^{(V+10.66)/-11.1})} \tag{57}$$

and

$$\beta_j = \frac{0.3 \times e^{(-2.535\times10^{-7}V)}}{1 + e^{(-0.1(V+32))}} \tag{58}$$

For V<-40 mV

$$\alpha_h = 0.135 \times e^{\left(80 + \frac{V}{-6.8}\right)} \tag{59}$$

and

$$\beta_h = 3.56 \times e^{(0.079V)} + 3.1 \times 10^5 \times e^{0.35V} \tag{60}$$

$$\alpha_j = \frac{-1.2714 \times 10^5 \times e^{0.244V} - 3.474 \times 10^{-5} \times e^{-0.04391V} \times (V + 37.78)}{1 + e^{0.311(V+79.23)}} \tag{61}$$

and

$$\beta_j = \frac{0.1212 \times e^{(-0.1052V)}}{1 + e^{(-0.1378(V+40.14))}} \tag{62}$$

$$\alpha_m = \frac{0.32 \times (V + 47.13)}{1 - e^{(-0.1(V+47.13))}} \tag{63}$$

and

$$\beta_m = 0.08 \times e^{\left(-\frac{V}{11}\right)} \tag{64}$$

L-type voltage gates Ca^{2+} channels have been found in human T cells [88]. The L-type calcium current also follows the formulation from the Luo-Rudy model given by

$$I_{CaL} = dff_{Ca}\overline{I_{CaL}} \tag{65}$$

where the maximal current $\overline{I_{CaL}}$, the activation gate d, and inactivation gate f, and Ca^{2+} inactivation gate f_{Ca} are described by

$$\overline{I_{CaL}} = P_{CaL}zF\frac{z^2F^2}{RT}\frac{\propto_{cyt} - \propto_o}{e^{\frac{zVF}{RT}} - 1} \tag{66}$$

$$f_{Ca} = \frac{1}{1 + \left([Ca^{2+}]_{cyt}/0.6\right)^2} \tag{67}$$

$$d_\infty = \frac{1}{1 + e^{\left(-\frac{(V+10)}{6.24}\right)}} \tag{68}$$

$$f_\infty = \frac{1}{1 + e^{\left(\frac{(V+35)}{8.6}\right)} + 0.6/\left(1 + e^{\left(\frac{(50-V)}{20}\right)}\right)} \tag{69}$$

$$\tau_d = \frac{d_\infty\left(1 - e^{\left(-\frac{(V+10)}{6.24}\right)}\right)}{0.35(V + 10)} \tag{70}$$

$$\tau_f = \frac{1}{0.0197e^{\left(-\left(0.0337(V+10)^2\right)+2\right)}} \tag{71}$$

The TRPM4 channel is a non-selective cation channel that is activated by calcium and membrane potential, For this model the formulation developed by Gaur and co-workers was used [30]:

$$I_{TRPM4} = g_{TRPM4}x_{Cai}x_v(V - E_{TRPM4}) \tag{72}$$

$$\frac{dx_{Ca}}{dt} = \frac{x_{Ca\infty} - x_{Ca}}{\tau_{xCai}} \tag{73}$$

$$x_{Ca\infty} = \frac{1}{1 + \left([Ca^{2+}]_{cyt}/1.3\right)^{-1.1}} \tag{74}$$

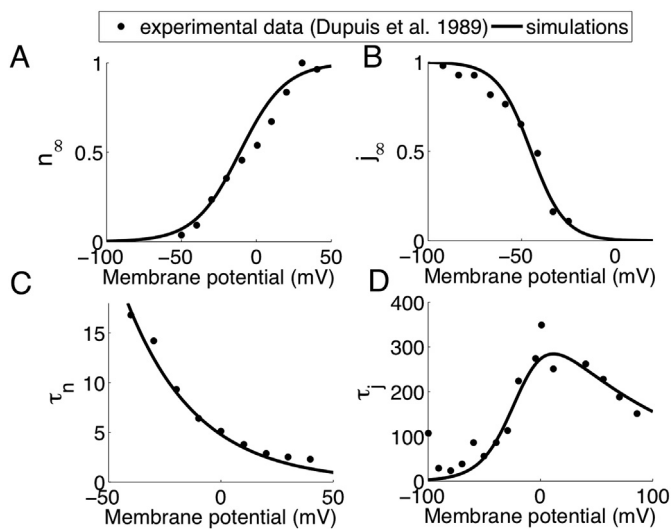$$x_v = 0.05 + \frac{0.95}{1 + e^{-((V+40)/15)}} \tag{75}$$

Figure 16. Experimental (symbols) and model optimized (lines) I_K current. (A) I_K current activation and (B) inactivation curves. (C) n-gate and j-gate (D) time constants.

where E_{TRPM4} is the reversal potential, g_{TRPM4} is the conductance, and τ_{xCa} is the Hodgkin-Huxley time constant.

The TRPC3 channel conducts Ca^{2+} and is activated by diacyl glycerol (DAG) with a roughly linear I–V relation [31].

$$I_{TRPC3} = g_{TRPC3} \frac{[DAG]}{[DAG] + K_{DAG}} (V - E_{Ca}) \tag{76}$$

where K_{DAG} is the activation constant for DAG binding to the channel.

The chloride current (I_{Cl}) is described by

$$I_{Cl} = g_{Cl}(V - E_{Cl}) \tag{77}$$

where g_{Cl} is the Cl^- channel conductance and E_{Cl} is the reversal potential for Cl^-.

The [DAG] is produced by phospholipase C from the cleavage of PIP_2 and thus has the same production rate (v_4) as IP_3. It is assumed to decay with first order kinetics with rate constant v_{DAGdeg}.

$$\frac{d[DAG]}{dt} = v_4 - v_{DAGdeg}[DAG] \tag{78}$$

The membrane potential equation is given by

$$\frac{dV}{dt} = \frac{-1}{C_m}\left(I_K + I_{K(Ca)} + I_{Na} + I_{CRAC} + I_{pmca} + I_{CaL} + I_{TRPM4} + I_{TRPC3} + I_{Cl}\right) \tag{79}$$

where C_m is the membrane capacitance.

In the simulations used to study NFAT and NFκB activation, we incorporated the NFAT and NFκB activation pathways described by Fisher and co-workers [63] into this cytosolic Ca^{2+} transients model. The NFAT model has a modification to activation of calmodulin by Ca^{2+} to represent the 2 high and 2 low affinity binding sites of calmodulin replacing the dependence on $[Ca^{2+}]^3$ in that model by the equation

$$20.0 \frac{[Ca^{2+}]^2}{[Ca^{2+}]^2 + (1.0\mu M)^2} \frac{[Ca^{2+}]^2}{[Ca^{2+}]^2 + (10.0\mu M)^2} \tag{80}$$

To study JNK activation, the cytosolic Ca^{2+} transients generated by this model were used as inputs for the model of JNK activation. Using the law of mass action, the reaction scheme in Figure 9A yields a system of 3 coupled first order differential equations.

$$\frac{df_{JNK:Cn}}{dt} = k_1(1 - f_{JNK:Cn} - f_{JNK:PKC} - f_{JNK:PKC:Cn})[C^*_c] - k_2 f_{JNK:Cn}$$
$$+ k_8 f_{JNK:PKC:Cn} - k_7 f_{JNK:Cn}[PKC\theta *] \tag{81}$$

$$\frac{df_{JNK:PKC}}{dt} = k_3(1 - f_{JNK:Cn} - f_{JNK:PKC} - f_{JNK:PKC:Cn})[PKC\theta *] - k_4 f_{JNK:PKC}$$
$$+ k_6 f_{JNK:PKC:Cn} - k_5 f_{JNK:PKC}[C^*_c] \tag{82}$$

$$\frac{df_{JNK:PKC:Cn}}{dt} = k_5 f_{JNK:PKC}[C^*_c] - k_6 f_{JNK:PKC:Cn} + k_7 f_{JNK:Cn}[PKC\theta *]$$
$$- k_8 f_{JNK:PKC:Cn} \tag{83}$$

The model simulates the JNK activation pathways that are involved in the activation of transcription factor AP-1 in T lymphocytes. AP-1 binds to promoter regions of DNA with transcription factors NFAT and NFκB initiating new gene transcription results in cell proliferation and differentiation [23].

Many studies have shown that PKCs and calcineurin act as co-activators of JNK leading to phosphorylation of c-Jun. Figure 9B shows that the percent active JNK in the cytoplasm falls rapidly when PKCθ concentrations are low, which agrees with the experimental results shown in Leung and co-workers [44]. As in experiment, with activation the phosphorylated JNK reaches a maximum at about 30 min, declines to half maximum at about 45 min and is close to zero after 2 h.

Avraham and colleagues [20] suggest that calcineurin and PKCθ must co-stimulate to reach full activation of JNK. A high calcineurin concentration does not activate JNK. On the other hand, high PKCθ concentration can induce about 50% JNK activation. Figure 9C shows that the fold activation only reached to 1 with calcineurin, and that fold activation is 8.7 with PKCθ, which matches with the experimental data shown [20].

4.2. Sensitivity analysis

A sensitivity analysis was performed to demonstrate how NFAT activation depended upon model parameters (Figure 14). Sensitivity was calculated by:

$$\frac{\ln\left(\frac{\text{fre. of UDB at } +10\%}{\text{fre. of UDB at } -10\%}\right)}{\ln\left(\frac{\text{rate at } +10\%}{\text{rate at } -10\%}\right)} \tag{84}$$

The parameters controlling CRAC current, K^+ currents, and membrane potential show the greatest effect on active NFAT. Upon further exploration, the model suggests CRAC current is essential for the elevation in cytosolic Ca^{2+} sufficiently to activate NFAT. Hence increasing the Ca^{2+} entry via CRAC enhances NFAT activation. Reduction of the membrane potential serves to reduce CRAC current making it an important parameter. Therefore, K^+ current that help to maintain the membrane potential by opposing depolarization by CRAC are necessary to maintain sufficient driving force for Ca^{2+} entry to activate NFAT. These studies suggest the important components for T cell activation.

4.3. Numerical methods

The differential equations defining the model were solved using Euler's Method with a fixed time step of 0.01 s. The computer program was written in FORTRAN and run on Linux workstations. Numerical results were visualized using MATLAB 7.0.1 by The MathWorks, Inc.

Model parameters may be loosely divided into three groups: 1) derived from published data, 2) estimated from published data so that model variable value and time course conformed to experimental data, and 3) fitted specific model equations to experimental data.

Declarations

Author contribution statement

Pei-Chi Yang: Conceived and designed the experiments; Performed the experiments; Analyzed and interpreted the data; Wrote the paper.

M. Saleet Jafri: Conceived and designed the experiments; Performed the experiments; Analyzed and interpreted the data; Contributed reagents, materials, analysis tools or data; Wrote the paper.

Competing interest statement

The authors declare no conflict of interest.

Additional information

Supplementary content related to this article has been published online at https://doi.org/10.1016/j.heliyon.2020.e03526.

Acknowledgements

References

[1] M.J. Berridge, A. Galione, Cytosolic calcium oscillators, Faseb. J. 2 (15) (1988) 3074–3082. PubMed PMID: 2847949.

[2] M.S. Jafri, J. Keizer, On the roles of Ca2+ diffusion, Ca2+ buffers, and the endoplasmic reticulum in IP3-induced Ca2+ waves, Biophys. J. 69 (5) (1995) 2139–2153. PubMed PMID: 8580358.

[3] K. Kalman, M.W. Pennington, M.D. Lanigan, A. Nguyen, H. Rauer, V. Mahnir, et al., ShK-Dap22, a potent Kv1.3-specific immunosuppressive polypeptide, J. Biol. Chem. 273 (49) (1998) 32697–32707. PubMed PMID: 9830012.

[4] G. Panyi, Z. Varga, R. Gaspar, Ion channels and lymphocyte activation, Immunol. Lett. 92 (1-2) (2004) 55–66. PubMed PMID: 15081528.

[5] S. Srivastava, Z. Li, K. Ko, P. Choudhury, M. Albaqumi, A.K. Johnson, et al., Histidine phosphorylation of the potassium channel KCa3.1 by nucleoside diphosphate kinase B is required for activation of KCa3.1 and CD4 T cells, Mol. Cell 24 (5) (2006) 665–675. PubMed PMID: 17157250.

[6] S. Grissmer, A.N. Nguyen, M.D. Cahalan, Calcium-activated potassium channels in resting and activated human T lymphocytes. Expression levels, calcium dependence, ion selectivity, and pharmacology, J. Gen. Physiol. 102 (4) (1993) 601–630. PubMed PMID: 7505804.

[7] M. Trebak, J.-P. Kinet, Calcium signalling in T cells, Nat. Rev. Immunol. 19 (3) (2019) 154–169.

[8] S. Feske, H. Wulff, E.Y. Skolnik, Ion channels in innate and adaptive immunity, Annu. Rev. Immunol. 33 (2015) 291–353. Epub 2015/04/12, PubMed PMID: 25861976; PubMed Central PMCID: PMCPMC4822408.

[9] R.S. Lewis, Calcium signaling mechanisms in T lymphocytes, Annu. Rev. Immunol. 19 (2001) 497–521. PubMed PMID: 11244045.

[10] M. Hoth, D.C. Button, R.S. Lewis, Mitochondrial control of calcium-channel gating: a mechanism for sustained signaling and transcriptional activation in T lymphocytes, Proc. Natl. Acad. Sci. U. S. A. 97 (19) (2000) 10607–10612. PubMed PMID: 10973476.

[11] C. Loh, K.T. Shaw, J. Carew, J.P. Viola, C. Luo, B.A. Perrino, et al., Calcineurin binds the transcription factor NFAT1 and reversibly regulates its activity, J. Biol. Chem. 271 (18) (1996) 10884–10891. PubMed PMID: 8631904.

[12] V.A. Ruff, K.L. Leach, Direct demonstration of NFATp dephosphorylation and nuclear localization in activated HT-2 cells using a specific NFATp polyclonal antibody, J. Biol. Chem. 270 (38) (1995) 22602–22607. PubMed PMID: 7545680.

[13] S. Wesselborg, D.A. Fruman, J.K. Sagoo, B.E. Bierer, S.J. Burakoff, Identification of a physical interaction between calcineurin and nuclear factor of activated T cells (NFATp), J. Biol. Chem. 271 (3) (1996) 1274–1277. PubMed PMID: 8576111.

[14] M. Vaeth, S. Feske, NFAT control of immune function: new frontiers for an abiding trooper, F1000Res. 7 (2018) 260. Epub 2018/03/24, PubMed PMID: 29568499; PubMed Central PMCID: PMCPMC5840618.

[15] C.R. Beals, N.A. Clipstone, S.N. Ho, G.R. Crabtree, Nuclear localization of NF-ATc by a calcineurin-dependent, cyclosporin-sensitive intramolecular interaction, Genes Dev. 11 (7) (1997) 824–834. PubMed PMID: 9106655.

[16] K.T. Shaw, A.M. Ho, A. Raghavan, J. Kim, J. Jain, J. Park, et al., Immunosuppressive drugs prevent a rapid dephosphorylation of transcription factor NFAT1 in stimulated immune cells, Proc. Natl. Acad. Sci. U. S. A. 92 (24) (1995) 11205–11209. PubMed PMID: 7479966.

[17] P.A. Baeuerle, D. Baltimore, I kappa B: a specific inhibitor of the NF-kappa B transcription factor, Science 242 (4878) (1988) 540–546. PubMed PMID: 3140380.

[18] J.A. DiDonato, M. Hayakawa, D.M. Rothwarf, E. Zandi, M. Karin, A cytokine-responsive IkappaB kinase that activates the transcription factor NF-kappaB, Nature 388 (6642) (1997) 548–554. PubMed PMID: 9252186.

[19] F. Mercurio, H. Zhu, B.W. Murray, A. Shevchenko, B.L. Bennett, J. Li, et al., IKK-1 and IKK-2: cytokine-activated IkappaB kinases essential for NF-kappaB activation, Science 278 (5339) (1997) 860–866. PubMed PMID: 9346484.

[20] A. Avraham, S. Jung, Y. Samuels, R. Seger, Y. Ben-Neriah, Co-stimulation-dependent activation of a JNK-kinase in T lymphocytes, Eur. J. Immunol. 28 (8) (1998) 2320–2330. PubMed PMID: 9710210.

[21] A. Altman, M. Villalba, Protein kinase C-theta (PKC theta): a key enzyme in T cell life and death, J. Biochem. (Tokyo) 132 (6) (2002) 841–846. PubMed PMID: 12473184.

[22] M. Villalba, A. Altman, Protein kinase C-theta (PKCtheta), a potential drug target for therapeutic intervention with human T cell leukemias, Curr. Cancer Drug Targets 2 (2) (2002) 125–137. PubMed PMID: 12188914.

[23] C. Janeway, Immunobiology: the Immune System in Health and Disease, sixth ed., xxiii, Garland Science, New York, 2005, p. 823.

[24] R.E. Dolmetsch, K. Xu, R.S. Lewis, Calcium oscillations increase the efficiency and specificity of gene expression, Nature 392 (6679) (1998) 933–936. PubMed PMID: 9582075.

[25] R.E. Dolmetsch, R.S. Lewis, Signaling between intracellular Ca2+ stores and depletion-activated Ca2+ channels generates [Ca2+]i oscillations in T lymphocytes, J. Gen. Physiol. 103 (3) (1994) 365–388. PubMed PMID: 8195779.

[26] D.M. Bautista, M. Hoth, R.S. Lewis, Enhancement of calcium signalling dynamics and stability by delayed modulation of the plasma-membrane calcium-ATPase in human T cells, J. Physiol. 541 (Pt 3) (2002) 877–894. PubMed PMID: 12068047.

[27] S. Swillens, D. Mercan, Computer simulation of a cytosolic calcium oscillator, Biochem. J. 271 (3) (1990) 835–838. PubMed PMID: 2244883.

[28] G. Dupuis, J. Heroux, M.D. Payet, Characterization of Ca2+ and K+ currents in the human Jurkat T cell line: effects of phytohaemagglutinin, J. Physiol. 412 (1989) 135–154. PubMed PMID: 2557424.

[29] J.A. Verheugen, H.P. Vijverberg, M. Oortgiesen, M.D. Cahalan, Voltage-gated and Ca(2+)-activated K+ channels in intact human T lymphocytes. Noninvasive measurements of membrane currents, membrane potential, and intracellular calcium, J. Gen. Physiol. 105 (6) (1995) 765–794. PubMed PMID: 7561743.

[30] N. Gaur, T. Hof, M. Hassaiguerre, E.J. Vigmond, Propagation failiure by TRPM4 overexpreission, Biophys. J. 116 (2019) 69–476.

[31] R.A. Rose, B. DD, M. MM, G. WR, Ca(2+) entry through TRP-C channels regulates fibroblast biology in chronic atrial fibrillation, Circulation 126 (17) (2012) 2039–2041.

[32] C.H. Luo, Y. Rudy, A dynamic model of the cardiac ventricular action potential. I. Simulations of ionic currents and concentration changes, Circ. Res. 74 (6) (1994) 1071–1096. Epub 1994/06/01. PubMed PMID: 7514509.

[33] A. Quintana, D. Griesemer, E.C. Schwarz, M. Hoth, Calcium-dependent activation of T-lymphocytes, Pflügers Archiv 450 (1) (2005) 1–12. PubMed PMID: 15806400.

[34] G.R. Crabtree, Calcium, calcineurin, and the control of transcription, J. Biol. Chem. 276 (4) (2001) 2313–2316. PubMed PMID: 11096121.

[35] N.A. Clipstone, G.R. Crabtree, Identification of calcineurin as a key signalling enzyme in T-lymphocyte activation, Nature 357 (6380) (1992) 695–697. PubMed PMID: 1377362.

[36] S.J. O'Keefe, J. Tamura, R.L. Kincaid, M.J. Tocci, E.A. O'Neill, FK-506- and CsA-sensitive activation of the interleukin-2 promoter by calcineurin, Nature 357 (6380) (1992) 692–694. PubMed PMID: 1377361.

[37] A. Kiani, A. Rao, J. Aramburu, Manipulating immune responses with immunosuppressive agents that target NFAT, Immunity 12 (4) (2000) 359–372. PubMed PMID: 10795734.

[38] J. Aramburu, M.B. Yaffe, C. Lopez-Rodriguez, L.C. Cantley, P.G. Hogan, A. Rao, Affinity-driven peptide selection of an NFAT inhibitor more selective than cyclosporin A, Science 285 (5436) (1999) 2129–2133. PubMed PMID: 10497131.

[39] K.L. Abbott, B.B. Friday, D. Thaloor, T.J. Murphy, G.K. Pavlath, Activation and cellular localization of the cyclosporine A-sensitive transcription factor NF-AT in skeletal muscle cells, Mol. Biol. Cell 9 (10) (1998) 2905–2916. PubMed PMID: 9763451.

[40] Z. Xu, D. Zhang, X. He, Y. Huang, H. Shao, Transport of calcium ions into mitochondria, Curr. Genom. 17 (3) (2016) 215–219. Epub 2016/06/03, PubMed PMID: 27252588; PubMed Central PMCID: PMCPMC4869008.

[41] M. Graber, L.K. Bockenstedt, A. Weiss, Signaling via the inositol phospholipid pathway by T cell antigen receptor is limited by receptor number, J. Immunol. 146 (9) (1991) 2935–2943.

[42] R.Y. Tsien, T. Pozzan, T.J. Rink, T-cell mitogens cause early changes in cytoplasmic free Ca2+ and membrane potential in lymphocytes, Nature 295 (5844) (1982) 68–71. PubMed PMID: 6799829.

[43] E. Donnadieu, D. Cefai, Y.P. Tan, G. Paresys, G. Bismuth, A. Trautmann, Imaging early steps of human T cell activation by antigen-presenting cells, J. Immunol. 148 (9) (1992) 2643–2653. PubMed PMID: 1349319.

[44] C.Y. Leung, L. Liu, R.N. Wong, Y.Y. Zeng, M. Li, H. Zhou, Saikosaponin-d inhibits T cell activation through the modulation of PKCtheta, JNK, and NF-kappaB transcription factor, Biochem. Biophys. Res. Commun. 338 (4) (2005) 1920–1927. PubMed PMID: 16289105.

[45] J. Lam, H. Wulff, The lymphocyte potassium channels Kv1.3 and KCa3.1 as targets for immunosuppression, Drug Dev. Res. 72 (7) (2011) 573–584. Epub 2012/01/14, PubMed PMID: 22241939; PubMed Central PMCID: PMCPMC3253356.

[46] N. Zhao, Q. Dong, X.X. Fu, L.L. Du, X. Cheng, Y.M. Du, et al., Acacetin blocks kv1.3 channels and inhibits human T cell activation, Cell. Physiol. Biochem. 34 (4) (2014) 1359–1372. Epub 2014/10/11, PubMed PMID: 25301362.

[47] E.Y. Chiang, T. Li, S. Jeet, I. Peng, J. Zhang, W.P. Lee, et al., Potassium channels Kv1.3 and KCa3.1 cooperatively and compensatorily regulate antigen-specific memory T cell functions, Nat. Commun. 8 (2017) 14644. https://www.nature.com/articles/ncomms14644#supplementary-information.

[48] J.H. Sim, K.S. Kim, H. Park, K.J. Kim, H. Lin, T.J. Kim, et al., Differentially expressed potassium channels are associated with function of human effector memory CD8(+) T cells, Front. Immunol. 8 (2017) 859. Epub 2017/08/10, PubMed PMID: 28791017; PubMed Central PMCID: PMCPMC5522836.

[49] P. Launay, H. Cheng, S. Srivatsan, R. Penner, A. Fleig, J.P. Kinet, TRPM4 regulates calcium oscillations after T cell activation, Science 306 (5700) (2004) 1374–1377. Epub 2004/11/20, PubMed PMID: 15550671.

[50] A. Parenti, F. De Logu, P. Geppetti, S. Benemei, What is the evidence for the role of TRP channels in inflammatory and immune cells? Br. J. Pharmacol. 173 (6) (2016) 953–969. Epub 2015/11/26, PubMed PMID: 26603538; PubMed Central PMCID: PMCPMC5341240.

[51] S. Bertin, E. Raz, Transient receptor potential (TRP) channels in T cells, Semin. Immunopathol. 38 (3) (2016) 309–319. Epub 2015/10/16, PubMed PMID: 26468011; PubMed Central PMCID: PMCPMC4833713.

[52] S. Philipp, B. Strauss, D. Hirnet, U. Wissenbach, L. Mery, V. Flockerzi, et al., TRPC3 mediates T-cell receptor-dependent calcium entry in human T-lymphocytes, J. Biol. Chem. 278 (29) (2003) 26629–26638. Epub 2003/05/09, PubMed PMID: 12736256.

[53] R.S. Lacruz, S. Feske, Diseases caused by mutations in ORAI1 and STIM1, Ann. N. Y. Acad. Sci. 1356 (2015) 45–79. Epub 2015/10/16, PubMed PMID: 26469693; PubMed Central PMCID: PMCPMC4692058.

[54] S. Naghdi, M. Waldeck-Weiermair, I. Fertschai, M. Poteser, W.F. Graier, R. Malli, Mitochondrial Ca^{2+} uptake and not mitochondrial motility is required for STIM1-

Orai1-dependent store-operated Ca^{2+} entry, J. Cell Sci. 123 (15) (2010) 2553–2564.

[55] A.T. Deak, S. Blass, M.J. Khan, L.N. Groschner, M. Waldeck-Weiermair, S. Hallstrom, et al., IP3-mediated STIM1 oligomerization requires intact mitochondrial Ca2+ uptake, J. Cell Sci. 127 (Pt 13) (2014) 2944–2955. Epub 2014/05/09, PubMed PMID: 24806964; PubMed Central PMCID: PMCPMC4077590.

[56] X. Li, G. Wu, Y. Yang, S. Fu, X. Liu, H. Kang, et al., Calmodulin dissociates the STIM1-Orai1 complex and STIM1 oligomers, Nat. Commun. 8 (1) (2017) 1042.

[57] F.M. Mullins, C.Y. Park, R.E. Dolmetsch, R.S. Lewis, STIM1 and calmodulin interact with Orai1 to induce Ca2+-dependent inactivation of CRAC channels, Proc. Natl. Acad. Sci. U. S. A. 106 (36) (2009) 15495–15500. Epub 2009/08/27, PubMed PMID: 19706428; PubMed Central PMCID: PMCPMC2741279.

[58] T. Ben-Kasus Nissim, X. Zhang, A. Elazar, S. Roy, J.A. Stolwijk, Y. Zhou, et al., Mitochondria control store-operated Ca(2+) entry through Na(+) and redox signals, EMBO J. 36 (6) (2017) 797–815. Epub 2017/02/22, PubMed PMID: 28219928; PubMed Central PMCID: PMCPMC5350565.

[59] C. Schwindling, A. Quintana, E. Krause, M. Hoth, Mitochondria positioning controls local calcium influx in T cells, J. Immunol. 184 (1) (2010) 184–190. PubMed PMID: 19949095.

[60] A. Quintana, M. Pasche, C. Junker, D. Al-Ansary, H. Rieger, C. Kummerow, et al., Calcium microdomains at the immunological synapse: how ORAI channels, mitochondria and calcium pumps generate local calcium signals for efficient T-cell activation, EMBO J. 30 (17) (2011) 3895–3912. PubMed PMID: 21847095; PubMed Central PMCID: PMCPMC3209779.

[61] S.P. Fraser, J.K. Diss, L.J. Lloyd, F. Pani, A.M. Chioni, A.J. George, et al., T-lymphocyte invasiveness: control by voltage-gated Na+ channel activity, FEBS Lett. 569 (1-3) (2004) 191–194. Epub 2004/07/01, PubMed PMID: 15225632.

[62] A.R. Patterson, M. Endale, K. Lampe, H.I. Aksoylar, A. Flagg, J.R. Woodgett, et al., Gimap5-dependent inactivation of GSK3β is required for CD4+ T cell homeostasis and prevention of immune pathology, Nat. Commun. 9 (1) (2018) 430.

[63] W.G. Fisher, P.C. Yang, R.K. Medikonduri, M.S. Jafri, NFAT and NFkappaB activation In T lymphocytes: a model of differential activation of gene expression, Ann. Biomed. Eng. 34 (11) (2006) 1712–1728. PubMed PMID: 17031595.

[64] L.E. Terry, K.J. Alzayady, E. Furati, D.I. Yule, Inositol 1,4,5-trisphosphate receptor mutations associated with human disease, Messenger (Los Angel) 6 (1-2) (2018) 29–44. Epub 2018/09/11. PubMed PMID: 30197841; PubMed Central PMCID: PMCPMC6128530.

[65] J.J. Rice, M.S. Jafri, R.L. Winslow, Modeling short-term interval-force relations in cardiac muscle, Am. J. Physiol. Heart Circ. Physiol. 278 (3) (2000) H913–H931. Epub 2000/03/10, PubMed PMID: 10710361.

[66] G.S. Williams, A.C. Chikando, H.T. Tuan, E.A. Sobie, W.J. Lederer, M.S. Jafri, Dynamics of calcium sparks and calcium leak in the heart, Biophys. J. 101 (6) (2011) 1287–1296. Epub 2011/09/29, PubMed PMID: 21943409; PubMed Central PMCID: PMCPMC3177068.

[67] S. Kim, S.M. Patrick, N.S. Braunstein, J.L. Thomas, E.F. Leonard, Modeling of early events in T cell signal transduction after controlled T cell activation by peptide major histocompatibility complex, Ann. Biomed. Eng. 29 (5) (2001) 373–383. PubMed PMID: 11400719.

[68] G. Desdín-Micó, G. Soto-Heredero, M. Mittelbrunn, Mitochondrial activity in T cells, Mitochondrion 41 (2018) 51–57.

[69] G.R. Bantug, M. Fischer, J. Grahlert, M.L. Balmer, G. Unterstab, L. Develioglu, et al., Mitochondria-endoplasmic reticulum contact sites function as immunometabolic hubs that orchestrate the rapid recall response of memory CD8(+) T cells, Immunity 48 (3) (2018) 542–555 e6. Epub 2018/03/11, PubMed PMID: 29523440; PubMed Central PMCID: PMCPMC6049611.

[70] S. Dimeloe, A.V. Burgener, J. Grahlert, C. Hess, T-cell metabolism governing activation, proliferation and differentiation; a modular view, Immunology 150 (1) (2017) 35–44. Epub 2016/08/02, PubMed PMID: 27479920; PubMed Central PMCID: PMCPMC5341500.

[71] N. Ron-Harel, A.H. Sharpe, M.C. Haigis, Mitochondrial metabolism in T cell activation and senescence: a mini-review, Gerontology 61 (2) (2015) 131–138. Epub 2014/11/18, PubMed PMID: 25402204.

[72] I.M.A. Wolf, A.H. Guse, Ca(2+) microdomains in T-lymphocytes, Front. Oncol. 7 (2017) 73. Epub 2017/05/18, PubMed PMID: 28512623; PubMed Central PMCID: PMCPMC5411426.

[73] J. Pettmann, A.M. Santos, O. Dushek, S.J. Davis, Membrane ultrastructure and T cell activation, Front. Immunol. 9 (2152) (2018).

[74] J.L. Dynes, A. Amcheslavsky, M.D. Cahalan, Genetically targeted single-channel optical recording reveals multiple Orai1 gating states and oscillations in calcium influx, Proc. Natl. Acad. Sci. U. S. A. 113 (2) (2016) 440–445. Epub 2015/12/30, PubMed PMID: 26712003; PubMed Central PMCID: PMCPMC4720334.

[75] J.U. Lee, L.K. Kim, J.M. Choi, Revisiting the concept of targeting NFAT to control T cell immunity and autoimmune diseases, Front. Immunol. 9 (2018) 2747. Epub 2018/12/13, PubMed PMID: 30538703; PubMed Central PMCID: PMCPMC6277705.

[76] N. Joseph, B. Reicher, M. Barda-Saad, The calcium feedback loop and T cell activation: how cytoskeleton networks control intracellular calcium flux, Biochim. Biophys. Acta 1838 (2) (2014) 557–568. Epub 2013/07/19, PubMed PMID: 23860253.

[77] P. Rangamani, M.G. Levy, S. Khan, G. Oster, Paradoxical signaling regulates structural plasticity in dendritic spines, Proc. Natl. Acad. Sci. U. S. A. 113 (36) (2016) E5298–E5307. Epub 2016/08/24, PubMed PMID: 27551076; PubMed Central PMCID: PMCPMC5018790.

[78] G.W. De Young, J. Keizer, A single-pool inositol 1,4,5-trisphosphate-receptor-based model for agonist-stimulated oscillations in Ca2+ concentration, Proc. Natl. Acad. Sci. U. S. A. 89 (20) (1992) 9895–9899. PubMed PMID: 1329108.

[79] J. Wagner, J. Keizer, Effects of rapid buffers on Ca2+ diffusion and Ca2+ oscillations, Biophys. J. 67 (1) (1994) 447–456. PubMed PMID: 7919018.

[80] M.S. Jafri, M. Kotulska, Modeling the mechanism of metabolic oscillations in ischemic cardiac myocytes, J. Theor. Biol. 242 (2006) 801–817.

[81] M.H. Nguyen, M.S. Jafri, Mitochondrial calcium signaling and energy metabolism, Ann. N. Y. Acad. Sci. 1047 (2005) 127–137. PubMed PMID: 16093491.

[82] S. Carrasco, T. Meyer, Cracking CRAC, Nat. Cell Biol. 12 (5) (2010) 416–418. Epub 2010/05/06, PubMed PMID: 20442700; PubMed Central PMCID: PMCPMC3897201.

[83] J. Pacheco, L. Vaca, STIM-TRP pathways and microdomain organization: auxiliary proteins of the STIM/orai complex, Adv. Exp. Med. Biol. 993 (2017) 189–210. Epub 2017/09/14, PubMed PMID: 28900915.

[84] A. Gudlur, A.E. Zeraik, N. Hirve, V. Rajanikanth, A.A. Bobkov, G. Ma, et al., Calcium sensing by the STIM1 ER-luminal domain, Nat. Commun. 9 (1) (2018) 4536.

[85] R.M. Luik, B. Wang, M. Prakriya, M.M. Wu, R.S. Lewis, Oligomerization of STIM1 couples ER calcium depletion to CRAC channel activation, Nature 454 (7203) (2008) 538–542. Epub 2008/07/04, PubMed PMID: 18596693; PubMed Central PMCID: PMCPMC2712442.

[86] S. Srikanth, K.D. Kim, Y. Gao, J.S. Woo, S. Ghosh, G. Calmettes, et al., A large Rab GTPase encoded by CRACR2A is a component of subsynaptic vesicles that transmit T cell activation signals, Sci. Signal. 9 (420) (2016) ra31. Epub 2016/03/27, PubMed PMID: 27016526; PubMed Central PMCID: PMCPMC5013727.

[87] S. Srikanth, H.J. Jung, K.D. Kim, P. Souda, J. Whitelegge, Y. Gwack, A novel EF-hand protein, CRACR2A, is a cytosolic Ca2+ sensor that stabilizes CRAC channels in T cells, Nat. Cell Biol. 12 (5) (2010) 436–446. Epub 2010/04/27, PubMed PMID: 20418871; PubMed Central PMCID: PMCPMC2875865.

[88] A. Badou, M.K. Jha, D. Matza, R.A. Flavell, Emerging roles of L-type voltage-gated and other calcium channels in T lymphocytes, Front. Immunol. 4 (2013) 243. Epub 2013/09/07, PubMed PMID: 24009608; PubMed Central PMCID: PMCPMC3757574.

[89] Y. Kirichok, G. Krapivinsky, D.E. Clapham, The mitochondrial calcium uniporter is a highly selective ion channel, Nature 427 (6972) (2004) 360–364. Epub 2004/01/23, PubMed PMID: 14737170.

[90] P. Paucek, M. Jaburek, Kinetics and ion specificity of Na(+)/Ca(2+) exchange mediated by the reconstituted beef heart mitochondrial Na(+)/Ca(2+) antiporter, Biochim. Biophys. Acta 1659 (1) (2004) 83–91. Epub 2004. PubMed PMID: 15511530.

[91] L. Skarka, B. Ostadal, Mitochondrial membrane potential in cardiac myocytes, Physiol. Res./Academia Scientiarum Bohemoslovaca 51 (5) (2002) 425–434. Epub 2002/12/10. PubMed PMID: 12470194.

[92] B.E. Corkey, J. Duszynski, T.L. Rich, B. Matschinsky, J.R. Williamson, Regulation of free and bound magnesium in rat hepatocytes and isolated mitochondria, J. Biol. Chem. 261 (6) (1986) 2567–2574.

[93] A. Zweifach, R.S. Lewis, Calcium-dependent potentiation of store-operated calcium channels in T lymphocytes, J. Gen. Physiol. 107 (5) (1996) 597–610. PubMed PMID: 8740373.

[94] A.M. Boesen, P. Hokland, Stereological analysis of the ultrastructure in isolated human T and non-T lymphoid cells. I. Description of method and data on normal blood lymphocytes, Virchows Arch. B Cell Pathol. Incl. Mol. Pathol. 39 (3) (1982) 273–284. PubMed PMID: 6126033.

[95] S. Feske, R. Draeger, H.H. Peter, K. Eichmann, A. Rao, The duration of nuclear residence of NFAT determines the pattern of cytokine expression in human SCID T cells, J. Immunol. 165 (1) (2000) 297–305. PubMed PMID: 10861065.